

# OptiMat Alloys: A FAIR End-to-End Agent with Living Database for Computational Multi-Principal Alloy Exploration

Yang Hu<sup>1,2,3</sup> and Vladyslav Turlo<sup>1,2,\*</sup>

<sup>1</sup>Laboratory for Advanced Materials Processing, Empa - Swiss Federal Laboratories for Materials Science and Technology, Feuerwerkerstrasse 39, 3602 Thun, Switzerland

<sup>2</sup>National Centre for Computational Design and Discovery of Novel Materials MARVEL, Empa, Thun, Switzerland

<sup>3</sup>Laboratory for Thin Films and Photovoltaics, Empa - Swiss Federal Laboratories for Materials Science and Technology, Ueberlandstrasse 129, Dübendorf, 8600, Switzerland

\*Corresponding author: Vladyslav Turlo, vladyslav.turlo@empa.ch

April 24, 2026

## Abstract

The FAIR principles have transformed how computational data and workflows are shared in materials research, yet existing repositories can only serve pre-computed entries—broad coverage is perpetually incomplete and cannot adapt to new questions on demand. To address these challenges, we present OptiMat Alloys, a large language model-powered conversational agent for multi-principal element alloy exploration built on three pillars: a *living database* that stores every calculation with provenance, *low-barrier accessibility* through a web interface requiring zero programming expertise, and *built-in uncertainty quantification* via cross-potential and cross-configuration validation (see demo here <https://youtu.be/1QzuorkzPMc>). Coupling foundational machine learning interatomic potentials covering near-all periodic table of elements with natural-language interaction, OptiMat Alloys enables targeted, on-demand computation guided by the user’s domain knowledge—extending FAIR from pre-computed repositories to on-demand knowledge generation and making computational alloy screening accessible to any materials scientist.

**Keywords**— FAIR principles, FAIR agents, materials informatics, LLM agents, multi-principal alloys, machine learning potentials

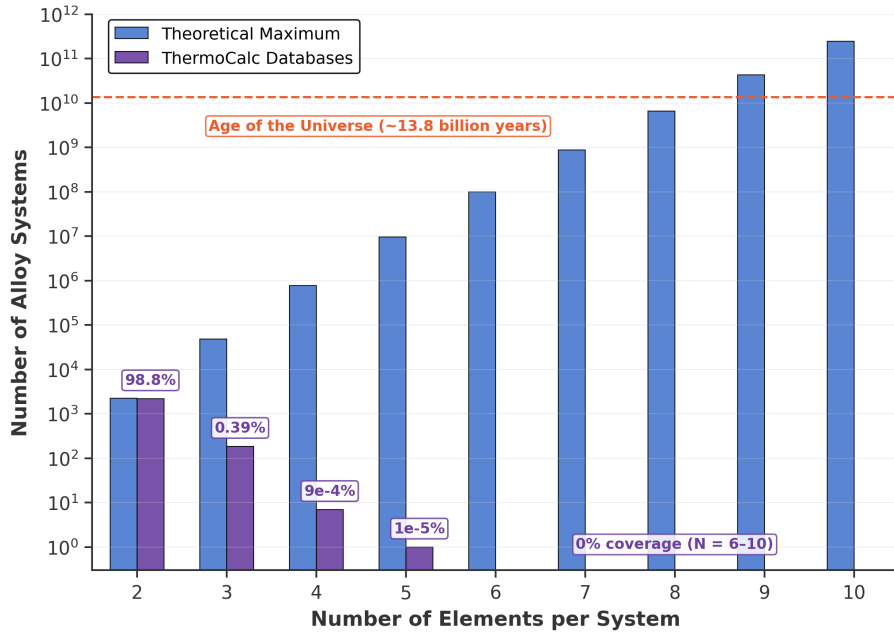
## 1. Introduction

The FAIR (Findable, Accessible, Interoperable, Reusable) principles have transformed how materials science shares and reuses data, particularly computational data [1, 2]. Repositories built on these principles—such as NOMAD [3, 2], Materials Project [4, 5], AFLOW [6], JARVIS [7], and Materials Cloud [8]—now collectively host millions of computed structures and properties, while workflow engines such as AiiDA enforce reproducibility by tracking every computational step from input to result [9]. The impact has been transformative: data-driven screening across these repositories has accelerated the identification of candidate materials for batteries, catalysts, and thermoelectrics, while machine learning models trained on database-scale density functional theory (DFT) data now predict stability and properties across broad regions of chemical space [2]. Together, these resources serve millions of queries annually and have become the bedrock of modern computational materials science—an unambiguous success story for sharing and reusing *existing* knowledge.

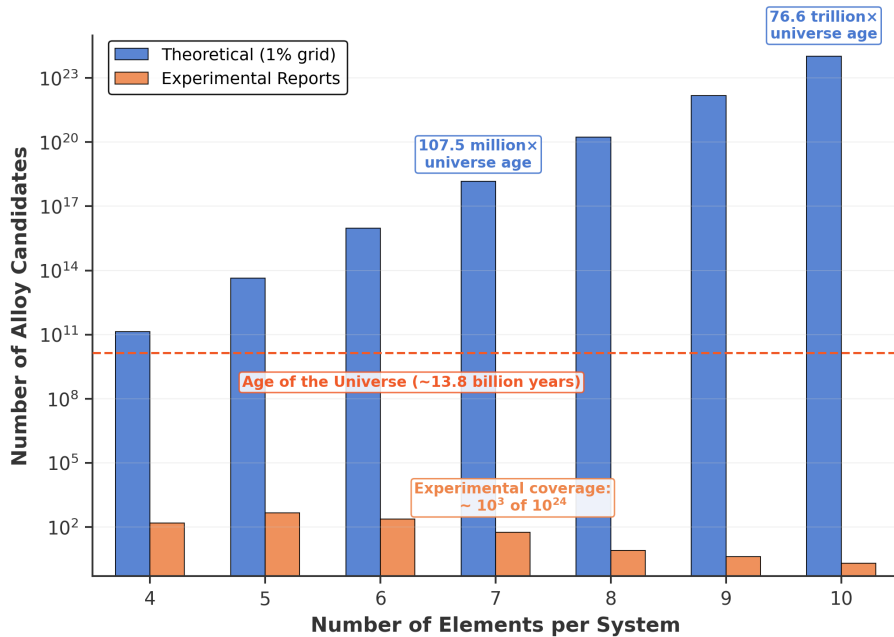
To populate these databases, data originate through three broad approaches: (i) dedicated team-driven pipelines (Materials Project [4], AFLOW [6], JARVIS [7]); (ii) community contributions with editorial review (Materials Cloud [8], MPContribs [10]); or (iii) open uploads with automated parsing (NOMAD [3])—the latter extended by a federated layer of local instances (Oases) that synchronize metadata with a central portal. In every case, only pre-computed entries can be queried; databases cannot generate new data in response to a new question. Some platforms go further: NOMAD’s integrated AI Toolkit can mine knowledge from existing entries [3], while its Remote Tools Hub (NORTH) and Materials Cloud provide browser-based simulation environments [3, 8]—yet these tools still require users to select appropriate codes, set input parameters, and interpret results, preserving the expertise barrier in performing simulations. Big data is commonly characterized along four dimensions—the so-called four Vs [2]: *volume* (the sheer number of entries), *variety* (the diversity of properties and material classes), *velocity* (the rate at which new data can be generated and served), and *veracity* (the reliability and reproducibility of results). Evaluated against these criteria, current materials databases can be further improved.

Current repositories appear impressive in volume and variety, yet that volume remains vanishingly small against the combinatorial design spaces of complex materials. Multi-principal element alloys (MPEAs), the focus of this work, illustrate this gap acutely. Their design demands exploration of systems with four or more constituent elements [11, 12], yet the number of possible alloy systems grows combinatorially while database coverage collapses. As Figure 1a shows, 67 metallic elements yield 2,211 binary but over 9.6 million quinary systems; our analysis of 16 Thermo-Calc thermodynamic databases [13] (as of October 2025; Supplementary Section S1.1) shows that CALPHAD assessments cover 98.8% of binaries yet only 0.0009% of quaternaries—with only the canonical Cantor alloy (CoCrFeMnNi) among all quinary possibilities—and even Materials Project’s catalogue spans <0.01% of possible alloy compositions. Figure 1b reveals an even starker reality—discretizing composition space at 1% resolution yields candidate sets reaching  $10^{54}$  for octonaries, while experimental reports span only  $\sim 1,000$  compositions across 4–10 elements [14] (see Supplementary Section S1.2).

Velocity is doubly constrained: contributions are limited to a small pool of researchers with simulation expertise, and even those specialists are throttled by manual setup, monitoring, and post-processing bottlenecks—after which results must still be formatted and deliberately deposited before they become discoverable. Veracity is no better: error estimates remain largely missing from computational results, yet are essential for interoperability with experiment [2]. Both precision—whether independent implementations reproduce one another—and accuracy—whether the underlying approximations capture the true physics—require systematic quantification. Bridging the gap between combinatorial demand and data supply requires a complementary, bottom-up mechanism that can generate, validate, and store new data on demand while lowering the simulation barrier so that domain experts—not only computation specialists—can contribute new entries, turning routine research interactions into persistent, provenance-rich records without deliberate deposition. Three capabilities, now mature enough to converge, make this extension feasible: well-established simulation codes and workflow engines, universal machine-learning interatomic potentials (U-MLIPs), and large-language-model (LLM)-powered AI agents that orchestrate them through natural language.



(a) Thermodynamic DB coverage vs theoretical systems



(b) Compositional explosion vs experimental coverage

Figure 1: The alloy design space dwarfs what is captured in thermodynamic databases and experiments. (a) Theoretical number of alloy systems grows combinatorially, while Thermo-Calc coverage collapses beyond ternaries (see Supplementary Section S1.1). (b) At 1% granularity, compositional candidates become astronomically large, whereas experimental reports span  $\sim 1$ k compositions across 4–10 elements (see Supplementary Section S1.2).

Common vision of *agentic computing*—in which large language models perceive context, reason over domain knowledge, plan multi-step workflows, and act on simulation tools through natural-language instruction [15, 16]—unites decades of infrastructure (Figure 2): atomistic simulation codes (VASP [17], LAMMPS [18]) and workflow engines (ASE [19], AiiDA [9]) that encode domain knowledge as Software 1.0 [20]—with the data-driven Software 2.0 paradigm [21], exemplified by U-MLIPs trained on vast DFT databases such as, ORB [22], NequIP [23], and MACE [24]. By

wrapping these capabilities in conversational agents (Software 3.0), one can encapsulate simulation and machine learning tools and workflows inside natural language-based interfaces with best practices in the field simply described to an agent through well-engineered system prompts and detailed tool descriptions. Unlike high-throughput campaigns that exhaustively map predetermined grids, such agents enable targeted, on-demand computation guided by the user’s own synthesis experience, phase-diagram intuition, or application requirements—exploring user-specified compositions and conditions on-demand rather than serving pre-tabulated results, so the new knowledge can be generated on the spot. Crucially, such agents need not merely *consume* FAIR data but can and should *embody* FAIR principles themselves [25].

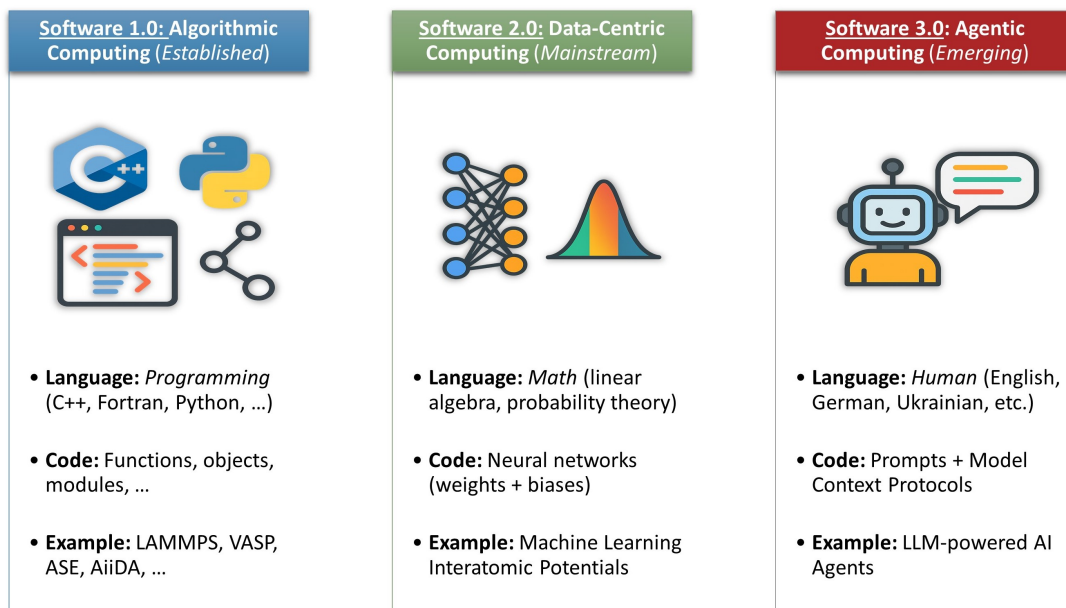


Figure 2: Paradigm evolution from algorithmic to agentic computing. Embedded in traditional simulation and workflow management codes (Software 1.0), U-MLIPs enable calculations for random alloys in realistic supercells at near-DFT fidelity on commodity hardware, while an AI agent (Software 3.0) wrap datasets with computation, provenance, and conversational workflows. OptiMat Alloys operationalizes this by retrieving prior knowledge, running new calculations when needed, and writing results back into a living database that grows through use.

Approximately twenty LLM-based agent prototypes have been reported in materials science and chemistry since 2023 [26, 27, 28, 29, 30, 31, 32] (Supplementary Table S16), spanning autonomous experiment design, chemical reasoning, and multi-step atomistic workflows. Encouragingly, most of these systems are open-source and publicly available, and generate traceable, reproducible computational data—reflecting a growing embrace of FAIR principles within the agentic computing community. Yet three barriers prevent on-demand computation from translating into cumulative, reliable knowledge. First, *ephemeral results*: none of the 20 surveyed systems writes computed results to a persistent, shared database; results are discarded after delivery or databases remain read-only, so every query starts from scratch and no collective map of composition space emerges. Second, *deployment barriers*: some surveyed systems require multi-step compilation, HPC access, or expert configuration, restricting access to the majority of materials scientists—experimentalists and domain specialists who possess deep knowledge of which compositions and properties deserve investigation but lack the programming expertise to act on that intuition computationally (Supplementary Table S16). Third, *absent uncertainty quantification*: surveyed agents that perform atomistic simulation rely on a single ML potential and a single structural realization, providing no built-in estimate of model or configurational uncertainty—users receive a number, not a confidence interval. These barriers compound—and map directly onto the four-V limitations identified above: on-demand computation without persistence constrains *volume*; restricted accessibility limits *velocity* by excluding the domain experts who could contribute; and absent uncertainty estimates undermine *veracity*, risking overconfidence in screening decisions.

Following this vision, we present **OptiMat Alloys**, a conversational research agent for multi-principal alloy discovery that addresses all three barriers. Built on U-MLIPs [22, 23, 24] that provide near-DFT accuracy across the periodic table, its architecture rests on three pillars. (1) A *living database* that complements top-down FAIR repositories [2] with a bottom-up data-generation pathway: every calculation is stored persistently with provenance tracking and search-based retrieval, so that the act of asking a question automatically produces FAIR-compliant data—eliminating the deliberate deposition step that currently bottlenecks community databases. (2) *Low-barrier accessibility* through a Chainlit [33] web interface that requires zero programming expertise, complemented by Docker containers for straightforward local deployment. (3) *Built-in uncertainty quantification* through three complementary mechanisms: cross-potential validation across multiple universal potentials (ORB, NequIP, MACE) brackets model uncertainty; cross-configuration comparison via multiple special quasi-random structure (SQS) realizations with distinct element distributions quantifies configurational sensitivity; and variable supercell sizes provide natural convergence checks—together yielding statistical confidence that emerges organically from routine use.

We argue that these three design choices are not engineering conveniences but *research contributions*—the living database determines what knowledge persists, lower-barrier accessibility determines who can contribute it, and built-in uncertainty quantification determines whether users can trust the results without external validation. Together, these contributions turn individually motivated queries into a collectively curated, self-growing map of the design space—one shaped by community priorities rather than a priori enumeration. In this way, OptiMat Alloys extends FAIR from pre-computed repositories to on-demand knowledge generation, making computational screening of the vast MPEA design space accessible to any materials scientist.

## 2. Results

This section presents OptiMat Alloys, an AI-native application for rapid computational screening of bulk quasi-random substitutional alloys using U-MLIPs. Section 2.1 describes and justifies the system architecture, the agent system prompt, and tool annotations. Section 2.2 validates the accuracy and performance of U-MLIPs against DFT and experiment. Section 2.3 contrasts the deployment barrier of OptiMat Alloys with that of other surveyed agents. Section 2.4 examines knowledge accumulation through use, and Section 2.5 demonstrates on-demand composition exploration through a case study anchored in CoCrFeNi and extending to the Co–Cr–Fe–Mo–Ni–W system.

### 2.1. Agent Architecture

Following the vision of the OptiMat Chat ecosystem (<https://www.optimat.chat/>), OptiMat Alloys encapsulates domain expertise, methodological capabilities, and best practices from computational materials science and agentic AI in a portable and downloadable framework. The codebase is implemented entirely in Python, a widely adopted high-level language for scientific software and workflows, as well as for both back-end and front-end development of AI agents. This design enables seamless integration, interoperability, and extensibility across a broad range of domains, including conventional simulation, analysis, and visualization tools, machine-learning workflows, database querying, and user-interface development. Its modular architecture also facilitates the reuse of individual components, such as helper functions, when constructing new agent tools.

For a given alloy composition and structure (face-centered cubic (FCC), body-centered cubic (BCC), hexagonal close-packed (HCP), simple cubic (SC), or diamond), OptiMat Alloys can compute: (i) formation energy and mixing enthalpy relative to elemental references, (ii) lattice parameters and mass density, (iii) full elastic tensors with Voigt–Reuss–Hill (VRH) polycrystalline moduli, and (iv) quasi-harmonic approximation (QHA) finite-temperature properties (Gibbs free energy, heat capacity, thermal expansion, bulk modulus vs. temperature). Structures are generated as SQS configurations to approximate the random solid solution. The intended use is computational exploration, screening, and hypothesis generation—ranking competing structure types, identifying composition–property trends, and flagging candidates for detailed DFT or experimental investigation—rather than definitive phase diagram prediction or quantitative thermodynamic assessment.

To deliver these capabilities, OptiMat Alloys integrates three software paradigms—traditional algorithms (Software 1.0), machine-learned models (Software 2.0), and AI agents that autonomously reason and act (Software 3.0; Fig. 2)—within a five-layer architecture (Fig. 3). The *interaction layer* provides a web-based chat interface with real-time task-progress indicators, Markdown tables, interactive Plotly charts [34], and OVITO-rendered structure images [35]. The *agent layer* hosts an AutoGen-based Scientist agent [36] that parses user intent, selects appropriate tools, fills in required inputs while requesting missing information when necessary, chains tools by passing outputs from one step as inputs to the next, and interprets results in scientific context. It supports multiple LLM providers, including OpenRouter [37] and Ollama [38], enabling both cloud-based and local models. The *tools layer* exposes seven specialized functions (Supplementary Table S14) spanning structure generation, property calculation, and database operations. The *core computation layer* implements atomistic simulation workflows, including SQS generation, two-stage relaxation, and property analysis. The *data layer* manages persistent SQLite storage with UUID-based organization, search-based retrieval, and full provenance tracking. Beyond providing a modular software stack, this architecture is designed to encode scientific best practices and technical safeguards directly into the execution logic of the system.

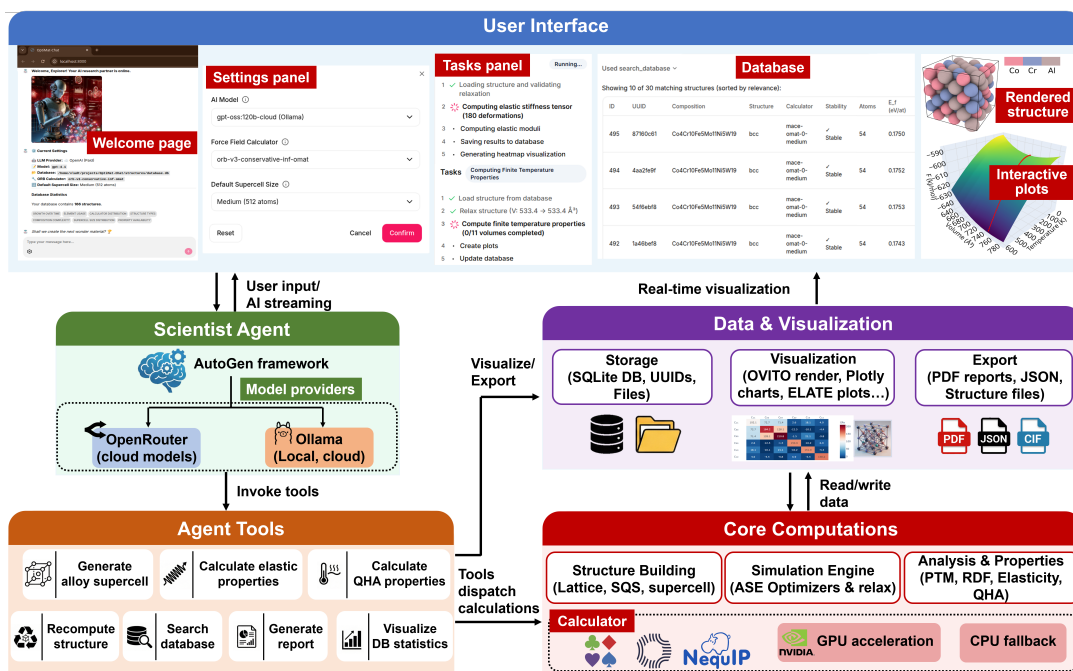


Figure 3: OptiMat Alloys’ five-layer system architecture. The demo is available at <https://youtu.be/IQzuorkzPMc>.

On the computational materials science side, domain-specific competencies and best practices are enforced by embedding validated simulation, analysis, and visualization procedures, together with critical parameters, directly within the agent tools, thereby placing them outside the agent’s discretionary control. For example, execution of the alloy supercell generation tool begins with construction of the specified unit cell, followed by determination of replication factors along each crystallographic direction through joint optimization of composition, total atom count, and supercell shape. Whereas the first two define a transparent numerical trade-off, with composition increments constrained by the inverse of the number of atoms, optimization of the supercell shape is introduced to preserve similarity to the parent unit cell. This reduces artifacts associated with periodic boundary conditions when the supercell is insufficiently extended along one or more dimensions. Such artifacts can limit the ability of the SQS algorithm to reproduce a representative random-alloy configuration and can also bias structural relaxation through spurious interactions between atoms and their periodic images. On the technical side, both numerical noise associated with GPU hardware and the rugged potential-energy landscapes characteristic of foundational machine-learned interatomic potentials are addressed through a two-stage relaxation protocol: an initial

coarse search for a low-energy configuration on GPU, followed by tighter convergence on CPU. This strategy balances computational efficiency and accuracy, while reserving CPU-based calculations for cases in which precise prediction of energy derivatives is essential for reliable property evaluation. Additional details are provided in the Methods section.

These safeguards are reinforced through the use of carefully selected default parameters within the agent tools wherever appropriate. These defaults, derived from extensive testing, are suitable for most common systems and user requests, while still allowing adaptive adjustment in edge cases where improved performance or reliability is required. For example, a default of one million SQS iterations is typically adequate for systems with up to four elements, but substantially larger iteration counts may be necessary for higher-order alloys to approach near-quasirandom configurations. Similarly, the default force-convergence threshold of 0.001 eV/Å during cell relaxation may be unnecessarily stringent for rapid interactive screening of compositional trends, particularly in large supercells. In the case of the lattice constant, a user-specified value is adopted when available; otherwise, a default value of 0.0 is used, triggering isotropic relaxation of the supercell from an initial estimate based on Vegard’s law. More broadly, OptiMat Alloys relies on explicit context engineering to support robust agent reasoning. Detailed parameter annotations, enforced defaults and boundary values, and clear specifications of tool outputs define the agent’s decision space, while raw simulation outputs are directed to the database and user interface rather than passed directly through the agent’s context window. Parameters that cannot be meaningfully defaulted, such as alloy composition and structure type, must instead be elicited from the user through conversation. By contrast, frequently reused session-level settings can be managed through the interface. For example, although the agent can change the universal MLIP upon request, such as for model-to-model comparison, the session default is specified in the user interface, thereby avoiding repeated user instruction for subsequent simulations. Likewise, users may modify the interatomic potential, the LLM provider or model, and the target atom count of the simulation cell during a session, with these changes communicated to the agent through dynamically injected system context (see Supplementary Section S2). In particular, control over the target atom count enables efficient transitions between exploratory calculations using small supercells and production-level calculations using medium or large supercells.

Beyond constraining the agent’s decision space through tool design, parameter annotations, and dynamic context management, OptiMat Alloys also governs agent behavior at the prompt level. All tools are attached to the Scientist agent through an extensive system prompt that defines the agent’s scope, priorities, and expected behavior (see Supplementary Section S2). The choice of a single specialized agent is motivated by recent advances in LLM capabilities that fundamentally change the architectural trade-offs of agentic systems. Early agentic systems commonly adopted multi-agent architectures involving planners, critics, orchestrators, and additional specialized tool-using agents. This complexity largely reflected the limitations of earlier LLMs, which operated primarily through single-pass text generation and were therefore more prone to hallucinations, planning errors, and inaccurate execution. As a result, iterative exchanges among multiple agents were often required to decompose user requests, verify intermediate reasoning, and determine appropriate actions. In parallel, the use of multiple execution agents was also motivated by the limited context windows of early models and their weak long-context retrieval capabilities, both of which impaired reliable adherence to system-level instructions and robust generation of structured outputs required for tool use. By contrast, modern reasoning models are capable of substantially more reliable internal deliberation, while recent instruction-tuned variants have been specifically optimized for instruction following and tool calling. Together with the expansion of context windows to scales approaching  $10^6$  tokens, these advances make it feasible for a single scope-specific agent to handle the full pipeline from request interpretation and action planning to tool execution, result synthesis, and scientific interpretation. In addition to reducing architectural complexity, the single-agent design improves debuggability and testing by concentrating control in a single system prompt and a well-defined set of tool annotations, thereby enabling more predictable behavior through prompt and context engineering.

Because this architecture places substantial responsibility on the underlying LLM, backend choice becomes a first-order design variable. Although the LLM-as-orchestrator design underpins nearly all agentic systems listed in Supplementary Table S16, few studies have systematically compared LLM backends with respect to scientific tool-calling reliability. This comparison is particularly

important because model capabilities evolve on the timescale of months, requiring agent frameworks to treat the LLM as a swappable module rather than a fixed dependency. OptiMat Alloys adopts this design principle through integration with OpenRouter and Ollama Cloud, both of which expose a broad range of advanced models through a unified API.

Our evaluation of six backends on a 10-test tool-calling suite (Supplementary Section S3, Table S5) reveals a clear pattern. The three top-performing models—GLM-4.5-Air, MiMo-V2-Flash, and GPT-OSS-120B, each scoring 95/100—are all reasoning-capable models that combine extended inference-time computation with large context windows [39, 40, 41]. By contrast, the paid conventional baseline GPT-4.1 [42], the strongest non-reasoning model considered here, scored 90/100. The five-point difference is concentrated in error-handling test E1, in which the model must recognize an ambiguous partial UUID and request clarification rather than invoking a tool prematurely, a behavior that benefits from deliberative reasoning rather than pattern matching alone. Model scale also contributes: GPT-OSS-20B (21 B parameters), despite being reasoning-capable, scored 90/100, compared with  $\geq 95/100$  for models with  $\geq 106$  B parameters, indicating that robust scientific tool-calling depends on both reasoning ability and sufficient scale. Notably, achieving this score with GPT-OSS-20B required substantial system-prompt engineering, including explicit specification of agent scope and detailed rules for tool selection, chaining, and request handling (see Supplementary Section S2). By contrast, the larger reasoning models required only a lightweight prompt defining the agent’s role as a simulation assistant and its expected behavior, including searching the database before launching new calculations, providing scientific interpretation of results, and terminating each completed interaction with a follow-up question.

At the same time, prompt engineering alone cannot overcome the practical limitations of smaller local models. Local deployment through Ollama represents an important step toward fully offline, privacy-preserving materials exploration. However, our tests show that a quantized GPT-OSS-20B model (MXFP4, 4,096-token context), requiring at least 16 GB of VRAM or system memory, achieves only 75/100—adequate for single-turn queries, but impractical for interactive multi-turn workflows. Two bottlenecks dominate: inference latency and context-window exhaustion. On CPU fallback, response times increase to 5–9 minutes, compared with 5–10 seconds through cloud deployment, while tool schemas alone consume approximately 25% of the 4,096-token budget, leaving insufficient room for sustained multi-turn interaction [43]. These results suggest that consumer-grade hardware is already sufficient for atomistic simulations with universal MLIPs, but remains inadequate for running local LLMs with the operating memory required for full agent functionality, particularly when LLM inference and U-MLIP calculations compete for the same GPU resources. By contrast, production-scale GPUs such as the A100 or H100 with 80 GB of VRAM should be able to support the agent at full capacity, enabling substantially longer context windows, larger model footprints, and sufficient K–V cache for efficient inference. The same class of hardware would also enable larger simulation cells for more accurate alloy-property calculations with universal MLIPs.

Despite these differences in backend capability and deployment feasibility, the execution model of OptiMat Alloys remains fundamentally request-driven. Guided by the system prompt, tool definitions, and conversational context. Upon receiving a query, the agent first determines whether the request falls within its scope. If so, it searches the database for relevant existing results before considering new calculations. When cached data are unavailable, the agent identifies which tools are required to address the request and determines whether essential inputs, such as composition or structure type, are missing. If additional information is needed, it elicits the missing parameters through dialogue. Otherwise, it proceeds with tool calling, chaining multiple tools when necessary and reasoning over intermediate outputs to decide subsequent actions. If tool execution fails or yields unphysical results, the agent informs the user and may propose alternative strategies. When successful, it returns the requested results together with scientific interpretation and relevant visualizations. In this way, the system supports flexible, request-dependent execution rather than a fixed computational pipeline.

## 2.2. Near-DFT Accuracy at Million-Fold Speedup

OptiMat Alloys achieves near-DFT accuracy at dramatically reduced computational cost through universal machine learning potentials. Table 1 compares wall-clock times for four U-MLIPs on equiatomic CoCrFeNi FCC supercells spanning 32 to 4,000 atoms, alongside VASP GPU timings for the three smallest sizes where DFT data are available. On an NVIDIA RTX 5000 Ada (16 GB)

Table 1: U-MLIP and VASP GPU runtime comparison on CoCrFeNi FCC supercells. Each value is the mean wall-clock time (ms) for a single forward pass (energy and forces), averaged over 100 repetitions after 5 warm-up passes. Device: NVIDIA RTX 5000 Ada, 16 GB. “OOM” = out-of-memory. Speedup is computed as VASP GPU wall time (single-point, NELM=60) divided by ORB Direct time; VASP did not reach SCF convergence (EDIFF=10<sup>-4</sup> eV) within 60 iterations, so reported times are *lower bounds* and speedup ratios are upper bounds. The 256-atom VASP entry is extrapolated from a single completed SCF iteration × 60; actual convergence may require more iterations.

System	Atoms	VASP GPU	U-MLIP Wall-Clock Time (ms)				Speedup
			ORB Direct	ORB Conserv.	MACE-OMAT-0	NequIP-OAM-XL	
2×2×2	32	11.6 min	0.10	0.09	0.09	0.10	~7,000×
3×3×3	108	79.5 min	0.10	0.10	0.09	0.11	~48,000×
4×4×4	256	3.78 days	0.10	0.10	0.10	0.11	~3.3M×
5×5×5	500	—	0.11	0.10	0.11	0.11	—
7×7×7	1372	—	0.12	0.12	0.11	OOM	—
9×9×9	2916	—	0.15	0.18	0.12	OOM	—
10×10×10	4000	—	0.20	OOM	0.14	OOM	—

— one of the top consumer-accessible GPU in 2025 for professional work, all four models evaluate energies and forces in a single forward pass, requiring approximately 0.10–0.20 ms per structure; at comparable system sizes their runtimes lie within 20% of each other, and both ORB v3 variants are essentially identical (~1–2% difference). For a 256-atom supercell, VASP requires at least 3.8 days for 60 SCF iterations (projected from a single completed iteration of 90.7 min), yet convergence may not be reached within this limit; ORB completes the same evaluation of system energy and atomic forces in 0.10 ms—a speedup exceeding six orders of magnitude. We emphasize that these ratios compare single-point energy evaluations at fixed atomic positions; they quantify the throughput advantage for screening workflows rather than implying equivalence of the two methods. DFT remains essential for properties beyond current MLIP scope—electronic structure, optical response, magnetic ground-state determination, etc.

Runtime is near-constant over this size range, with an effective scaling exponent  $\alpha \approx 0.09$ –0.15 in a power-law fit  $T(N) \propto N^\alpha$ , where  $\alpha$  is the slope of a log–log fit of wall-clock time versus atom count. For reference,  $\alpha = 1$  corresponds to linear scaling and  $\alpha = 3$  to the cubic cost of conventional DFT; exponents below ~0.2 mean that evaluation cost is effectively independent of system size (see Supplementary Section S4.2 for derivation and benchmark details including warmup exclusion and repeat statistics): a 125-fold increase in system size (32 to 4,000 atoms) increases evaluation time by only ~1.6×. These gains enable rapid screening and long molecular dynamics trajectories on commodity GPUs that would be impractical with traditional DFT workflows.

The U-MLIP models differ primarily in GPU memory requirements: NequIP-OAM-XL reaches out-of-memory at 1,372 atoms due to the E(3)-equivariant extra-large architecture, whereas MACE-OMAT-0 handles 4,000+ atoms without exceeding 16 GB—making the practical choice one of memory budget and accuracy characteristics rather than raw speed. We note that the NequIP timings in Table 1 are measured in-process within its dedicated environment; in production, NequIP runs via subprocess communication (requiring a separate conda environment), adding inter-process overhead that increases end-to-end relaxation times significantly for larger supercells.

Table 2 consolidates accuracy metrics across three validation tiers. On the Matbench Discovery benchmark (~257k diverse structures), the three tested models achieve energy-above-hull MAE below 30 meV/atom (Supplementary Table S8). Structure-matched elemental comparisons against OQMD DFT confirm lattice constant accuracy ( $R^2 = 0.95$ –0.97) and ground-state prediction rates of 79–89% (Supplementary Fig. S1, Table S9). These accuracies transfer to complex compositions: 28 binary and multi-component alloys yield lattice parameter MAE  $\leq 0.011$  Å and formation energy MAE  $\leq 0.014$  eV/atom relative to VASP (Supplementary Fig. S2). Experimental validation against 20 elemental metals confirms reproduction of bulk moduli, thermal expansion, and heat capacities within the ranges listed in Table 2 (Supplementary Tables S11–S13). Full details of benchmark methodology, per-model accuracy breakdowns, and cases of notable deviation from DFT (e.g., diamond-structure elements under MACE) are provided in Supplementary Section S4.3.

Table 2: Validation summary across three universal ML potentials. Elemental values are structure-matched comparisons against OQMD DFT ( $\sim 180$  data points). Alloy values are against VASP calculations on 28 binary and multi-component systems. Experimental values are against measurements on 20 elemental metals. Best/worst across calculators shown as ranges.

Category	Metric	Range (3 MLIPs)	Source
Elemental (vs. DFT)	Lattice constant MAE	0.09–0.12 Å	OQMD
	Lattice constant $R^2$	0.95–0.97	OQMD
	Ground-state accuracy	79–89%	OQMD
Alloy (vs. DFT)	Lattice parameter MAE	$\leq 0.011$ Å	VASP
	Formation energy MAE	$\leq 0.014$ eV/at	VASP
Thermo (vs. Expt.)	Bulk modulus MAE	16–25 GPa	[44]
	Thermal expansion MAE	$2.8\text{--}6.9 \times 10^{-6}$ K $^{-1}$	[45]
	Heat capacity MAE	$0.8\text{--}1.0$ J mol $^{-1}$ K $^{-1}$	[46]
Benchmark	$E_{\text{hull}}$ MAE	$< 30$ meV/at	Matbench Discovery

### 2.3. Ease of Deployment

Beyond computational performance, accessibility represents a critical contribution. To quantify installation difficulty across 20 LLM-based agent systems, we define an installation barrier score on a 1–10 scale reflecting the expertise required for a non-expert to achieve a working installation (full rubric in Supplementary Table S15): 1 (web-hosted: cloud platform, no local installation), 2 (turnkey: pre-built executable or Docker image, no coding), 3–4 (simple: single `pip install`, minimal configuration), 5–6 (multi-package: several dependencies or complex environment setup required), 7–8 (complex build: compilation from source, database setup, or HPC access), and 9–10 (expert: specialized hardware or proprietary software).

Supplementary Table S16 applies this rubric to 20 LLM-based agent systems for materials science and chemistry, comparing their simulation backends, user interfaces, installation methods, data persistence mechanisms, computational hardware requirements, code availability, and barrier scores. The surveyed systems span both domains: materials-science agents include alloy design tools (AtomAgents, LAMMPS-Agents), ML-potential platforms (LLaMP, LangSim, Crystalyse), and MOF discovery frameworks (ChatMOF), while chemistry agents cover quantum-chemical workflows (El Agente, Aitomia), solvation modelling (AutoSolvateWeb), and synthesis planning (ChemCrow); one system (SciToolAgent) spans biology, chemistry, and materials science. Of the 20, thirteen can execute atomistic or quantum-chemical simulations—using backends such as LAMMPS, ASE with MACE/ORB potentials, Quantum ESPRESSO, or ORCA—while the remaining seven, including MatAgent, HoneyComb, SciAgents, and Coscientist, focus on ML-based property prediction, knowledge-base retrieval and reasoning, or autonomous laboratory experiments without running physics-based simulations themselves. We restrict this comparison to LLM agent systems—tools that use large language models to orchestrate computational workflows—and exclude traditional databases (Materials Project, AFLOW) and workflow managers (AiiDA, Fireworks) that lack LLM-driven interfaces. Most surveyed systems provide conversational (natural language) user interfaces; two employ LLM orchestration with programmatic interfaces only (marked  $\dagger$  in Supplementary Table S16).

The 20 surveyed systems span barrier scores from 1 (web-hosted platforms) to 8 (systems requiring LAMMPS compilation or HPC access), with a mean of 4.8/10. Among the lowest-barrier systems, Aitomia and AutoSolvateWeb provide cloud-hosted quantum-chemistry workflows for molecular systems—solvation, spectra, reaction mechanisms—but do not target bulk crystalline materials; AGAPI-Agents performs cloud-hosted ML inference—ALIGNN-FF relaxation, GNN property prediction, and tight-binding band structures—across diverse material classes, though its cloud ALIGNN endpoint limits structures to 50 atoms; more broadly, cloud-hosted platforms may impose system-size and usage-rate constraints. At the other end, AtomAgents and LAMMPS-Agents (score 8) provide sophisticated multi-step workflows for experts willing to compile simulation engines and configure HPC environments. This score gap reflects a qualitative difference in required expertise: LAMMPS compilation from source demands a C++ compiler, MPI libraries, and a CMake build system, with dependency resolution that can consume hours and presupposes systems-

programming expertise absent from the typical materials-scientist skill set. OptiMat Alloys and LangSim share the lowest locally-deployed score (2/10), both offering single-command container deployment—a 2.8-point reduction from the counterpart average. The only additional step is registering for a free OpenRouter and Ollama Cloud API keys (no payment required to use free models, although limited number of requests per day); fully local deployment via Ollama eliminates API and registration, and our Docker image includes a bundled Ollama server, but this mode accepts reduced tool-calling reliability (Supplementary Section S3) unless production-scale GPU (A100 or H100) is installed on the machine. This gap in score translates to a qualitative accessibility difference: scores  $\leq 2$  require no programming expertise, while scores  $\geq 5$  presuppose familiarity with Python environments, package managers, and often domain-specific simulation codes.

## 2.4. Knowledge Accumulation Through Use

Low installation barriers and fast inference enable adoption, but their value compounds only when every computation is retained. OptiMat Alloys converts each conversational query into a persistent database entry, so the system’s knowledge base grows as a direct by-product of routine use. Search queries retrieve cached results instantly, while generation requests always produce new structures that are added to the database. Each entry stores far more than a single energy value: composition, structure type, lattice parameters, formation and mixing energies (relative to both ground-state and same-structure elemental references), mass density, and a polyhedral-template-matching (PTM) structural-fidelity score that quantifies how well the relaxed configuration retains the target crystal type. Entries generated by on-demand analysis tools additionally carry full elastic tensors with directional moduli, and quasi-harmonic finite-temperature properties (Gibbs free energy, heat capacity, thermal expansion, bulk modulus as functions of temperature). Full schema details are provided in Supplementary Section S6.1. Beyond computed properties, each entry retains full provenance metadata—calculator identity, version, and simulation parameters—so any result can be traced back to its exact computational conditions. A detailed simulation report, including structure visualizations, exportable files in CIF/POSCAR/CSV formats, and a bibliography of methods used, is generated on request, providing a self-contained reproducibility record (see Methods, Section 4.4). This dual storage of data and metadata aligns with FAIR principles: every entry is Findable (UUID plus searchable metadata), Accessible (local database with planned federation via collision-free identifiers), Interoperable (standard crystallographic file formats), and Reusable (full provenance enables independent verification). Together, this richness means the growing database functions as a queryable materials knowledge base—not merely an energy cache, but a FAIR-compliant research record. Figure 4 characterizes the database accumulated during six months of development and testing (October 2025 to April 2026).

The database grew to 491 structures across 54 active days (Fig. 4a), with a bursty pattern reflecting periods of intensive exploration separated by development intervals. The computational cost per entry is modest on a consumer GPU (NVIDIA RTX 5000 Ada, 16 GB): generating and relaxing a  $\sim 500$ -atom SQS supercell takes 3–7 min with MACE omat-0 and ORB v3 (Table 1). Full elastic-tensor calculations at 500 atoms add 20–30 min for MACE and ORB, while quasi-harmonic thermal properties require  $\sim 4$ –6 min per 48-atom cell and scale steeply with system size. Even including property calculations, the 491 entries represent on the order of a few hundred hours of cumulative GPU time, implying that a single researcher with dedicated use could generate hundreds of new entries per week. The architecture is also designed for decentralized scaling. Every entry carries a UUID4 identifier (see Methods), enabling collision-free merging of independently maintained databases without a central registry. In practice, this means that if  $N$  research groups each operate their own OptiMat Alloys instance, their local databases can be federated into a shared repository whose size grows as  $\sim N$  times the per-group contribution rate, covering far more of the vast combinatorial composition space (Fig. 1) than any single group could survey alone. The contribution here is the architecture for cumulative reuse, not the current database scale.

The composition complexity distribution (Fig. 4b) shows a broad spread across component counts. Systems with 6+ components form the largest single category (166 of 491 structures, 34%), followed by quaternary (136, 28%) and binary (127, 26%) entries, reflecting systematic exploration of Cantor-family alloy variants across multiple calculators and supercell sizes. Unary entries (19) serve as elemental references for formation energy calculations. Ternary (28) and quinary (11) systems round out the distribution. For each alloy composition, the system enables progressively

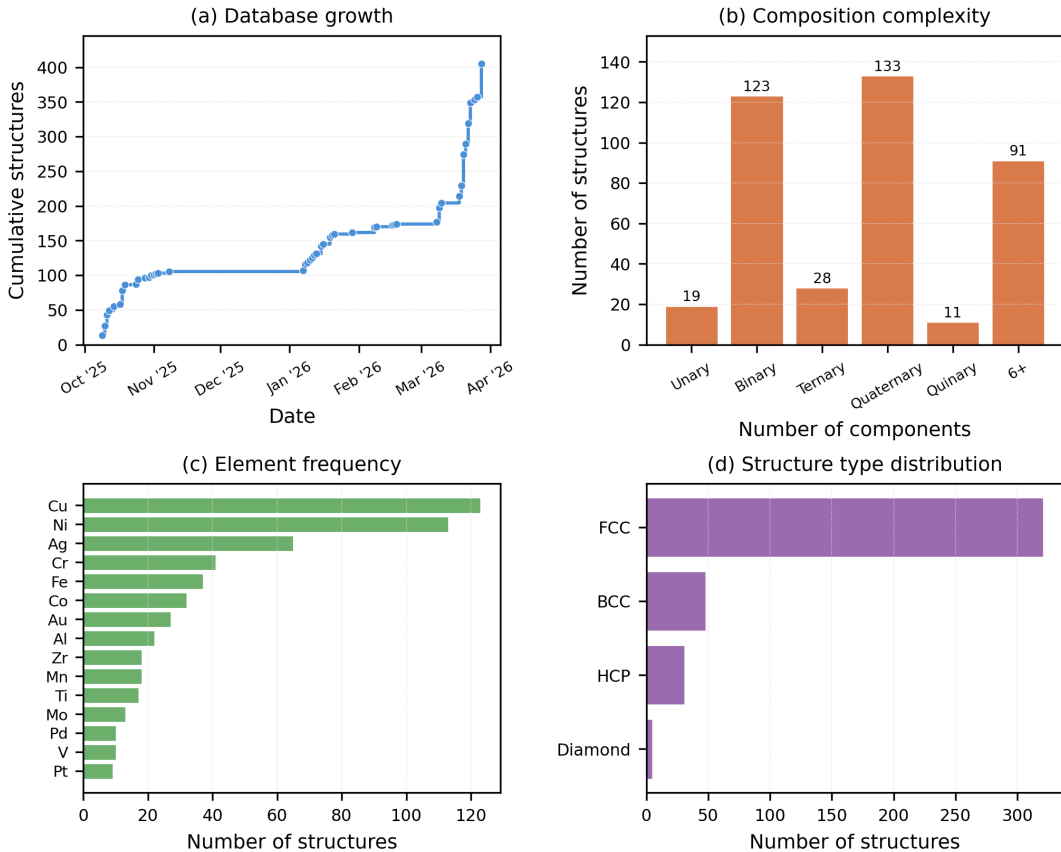


Figure 4: Database growth and composition statistics from OptiMat Alloys’s living database (491 structures, October 2025 to April 2026). (a) Cumulative database growth during development and testing, showing bursty accumulation across 54 active days. (b) Composition complexity distribution; 6+ component systems constitute the largest single category (34%), with substantial quaternary and binary populations. (c) Element frequency showing Cu and Ni as the most explored elements, reflecting Cu–Ni–X test systems and noble-metal alloys. (d) Structure type distribution showing FCC dominance (73%) consistent with MPEA research focus.

deeper characterization through three complementary axes. Users can select different supercell sizes (default  $\sim 500$  atoms; small  $\sim 48$ ; large  $\sim 2048$ ) to test convergence of computed properties with respect to cell dimensions, with small supercell used for quick exploration, while larger supercells used for production work. The same entry can be recomputed with different ML potentials (e.g. ORB, MACE, NequIP), producing independent entries that reveal calculator-dependent variation. Each SQS generation also yields a unique atomic arrangement, so repeated queries accumulate an ensemble of structures with slightly different element-site assignments—and consequently slightly different formation energies, elastic moduli, and other properties. Together, these axes allow users to assess size convergence, quantify inter-potential spread, and obtain mean property values with statistical error bars—uncertainty quantification that emerges organically from routine use rather than requiring bespoke convergence studies.

The element-frequency distribution (Fig. 4c) shows Cu and Ni as the most explored elements (125 and 117 appearances, respectively), consistent with Cu–Ni–X ternary systems and noble-metal alloys that served as primary test cases. Cr, Fe, and Co are also well-represented (44, 42, 35), reflecting Cantor-family alloy investigations. Structure types (Fig. 4d) are FCC-dominated (360 of 491, 73%), consistent with the prevalence of FCC solid solutions in MPEA research, with BCC (65) and HCP (61) providing secondary representation.

## 2.5. Case Study: From Validated Baseline to On-Demand Composition Exploration

Equiatomic FCC CoCrFeNi is the base quaternary of the Cantor family [11] and serves as a natural anchor for composition exploration. Starting from this well-characterized alloy, OptiMat Alloys enables on-demand exploration of how additional alloying elements affect structural and mechanical properties.

### 2.5.1. Properties of FCC SQS equiatomic CoCrFeNi

With abundant DFT and experimental reference data [47, 48, 49, 50], CoCrFeNi provides a stringent test. We benchmark OptiMat Alloys by generating fifteen independent SQS configurations at each of three supercell sizes (48, 500, and 2048 atoms) with three MLIP calculators—MACE omat-0, NequIP oam-xl, and ORB v3 conservative (NequIP is limited to  $\leq 500$ -atom cells due to GPU memory constraints on 16 GB hardware; see Table 1)—providing ensemble statistics for structural, mechanical, and thermal properties (Table 3).

Table 3 summarizes all computed properties alongside DFT and experimental references. All three calculators reproduce the DFT lattice parameter ( $a = 3.544$  Å; 108-atom SQS, VASP PBE-PAW) to within 0.4%. Formation energies are uniformly positive, consistent with our DFT value of 77.9 meV/atom and 76.7 meV/atom reported by Tamm et al. [51], indicating a metastable solid solution stabilized by configurational entropy. The  $\sim 10$  meV/atom spread among calculators likely reflects the difficulty of interpolating the magnetic energy landscape of CoCrFeNi from broad training sets, but remains within the  $\sim 30$  meV/atom accuracy typical of these models on the Matbench Discovery benchmark.

DFT elastic constants span a wide range depending on method (Table 3): values obtained by Exact Muffin-Tin Orbitals-Coherent Potential Approximation (EMTO-CPA) [52] are systematically higher than explicit VASP+SQS supercell calculations [52], and the latter are the most methodologically comparable reference for our MLIP results. Among the three calculators, MACE shows the closest agreement with VASP+SQS (e.g., matching  $C_{12}$  and  $K$  almost exactly), NequIP falls between VASP+SQS and EMTO-CPA, and ORB systematically underestimates all elastic constants. The Hill-averaged Young’s modulus from MACE and NequIP ( $E_{\text{VRH}} \approx 218\text{--}225$  GPa) falls within the DFT range of 195–225 GPa [52] and above experimental nanoindentation values ( $E = 172\text{--}208$  GPa) from as-milled powders [52] and sputtered thin films [53], which are expected to be lower due to finite-temperature softening, residual porosity, microstructural effects, and lattice strain in thin-film samples [54]. Overall, MACE best reproduces the VASP+SQS elastic constants and formation energy, while NequIP gives the closest lattice parameter.

Quasi-harmonic thermal property calculations (48-atom cells, limited by phonon cost on a consumer GPU) show all three calculators predict  $C_p \approx 0.42$  J g<sup>-1</sup> K<sup>-1</sup> (experiment:  $\sim 0.45$  [55]). For thermal expansion, MACE ( $\alpha = 15.2 \times 10^{-6}$  K<sup>-1</sup>) and ORB ( $14.9 \times 10^{-6}$  K<sup>-1</sup>) agree well with experiment ( $14.5 \times 10^{-6}$  K<sup>-1</sup> [55]), while NequIP underestimates at  $12.8 \times 10^{-6}$  K<sup>-1</sup>. The QHA bulk modulus at 300 K converges to  $\sim 167$  GPa for both MACE and NequIP, lower than the 0 K values (173 and 183 GPa) due to thermal softening.

A clear size-convergence trend is visible in Table 3: property means remain stable from 48 to 500 atoms, while ensemble standard deviations shrink substantially (e.g.,  $E_f$  spreads drop from  $\pm 2\text{--}4$  to  $\leq 1$  meV/atom between 48 and 500 atoms). Since mean values are largely independent of supercell size, 48-atom cells are sufficient for reliable bulk thermodynamic properties with accurate potentials such as MACE and NequIP.

### 2.5.2. Exploring the Co–Cr–Fe–Mo–Ni–W composition space

Wang et al. recently mapped phase stability, lattice parameters, hardness, and elastic modulus across the Co–Cr–Fe–Mo–Ni–W composition space using a combinatorial magnetron-sputtered thin-film library [56]. Two crystalline regions were identified: a nanostructured BCC phase near the W/Mo-rich compositions ( $a = 0.308\text{--}0.311$  nm,  $H = 7.8 \pm 0.3$  GPa,  $E = 199 \pm 8$  GPa) and an HCP phase near the Co/Ni-rich region ( $a = 0.251\text{--}0.252$  nm,  $c = 0.413\text{--}0.414$  nm,  $E = 152\text{--}168$  GPa). Computed bulk SQS properties for these six-component alloys—absent from existing computational databases—would provide an intrinsic reference against which thin-film measurements can be com-

Table 3: CoCrFeNi FCC properties from OptiMat Alloys using three MLIP calculators at multiple supercell sizes (averaged over 15 SQS configurations each except NequIP 500-atom elastic constants, which use 3 configurations), compared with DFT literature [52] and experimental thermal properties [55]. Property uncertainties are ensemble standard deviations in last digit(s).

Property	MACE		NequIP		ORB v3		DFT	Expt.
	48	500	48	500	48	500		
$a$ (Å)	3.531	3.531	3.547	3.547	3.539	3.539	3.544 <sup>a</sup>	—
$E_f$ (meV/at)	86(2)	85(1)	68(4)	68(1)	71(2)	70(1)	77.9 <sup>a</sup>	—
$C_{11}$ (GPa)	236(4)	234(1)	238(3)	239(0)	188(4)	188(1)	228 <sup>c</sup>	—
$C_{12}$ (GPa)	143(2)	143(1)	152(5)	155(1)	120(3)	121(1)	183 <sup>b</sup>	—
$C_{44}$ (GPa)	136(2)	135(1)	132(3)	132(1)	114(3)	113(1)	146 <sup>b</sup>	—
$K$ (GPa)	174(2)	173(1)	181(4)	183(0)	143(3)	144(1)	109 <sup>c</sup>	—
$E_{VRH}$ (GPa)	227(5)	225(2)	220(5)	218(1)	181(6)	179(2)	209 <sup>b</sup>	—
							172 <sup>c</sup>	—
							225 <sup>b</sup>	172 <sup>e</sup>
							195 <sup>c</sup>	208 <sup>f</sup>
<i>Thermal properties at 300 K (48-atom QHA)</i>								
$\rho$ (g/cm <sup>3</sup> )	8.37(1)		8.28(1)		8.37(1)		—	8.204 <sup>d</sup>
$\alpha$ (10 <sup>-6</sup> K <sup>-1</sup> )	15.2(2)		12.8(3)		14.9(4)		—	14.5 <sup>d</sup>
$C_p$ (J g <sup>-1</sup> K <sup>-1</sup> )	0.424(1)		0.423(1)		0.422(1)		—	0.45 <sup>d</sup>

<sup>a</sup>This work (VASP PBE-PAW, 108-atom SQS). <sup>b</sup>[52] (EMTO-CPA). <sup>c</sup>[52] (VASP+SQS).

<sup>d</sup>[55] (homogenized sample). <sup>e</sup>[52] (nanoindentation + VASP  $\nu$ ).

<sup>f</sup>[53] (nanoindentation, near-equiatom thin film).

pared to estimate the effects of residual stress, strain, nanocrystalline grain sizes, and porosity (4–8% area fraction) within the film.

We select two representative compositions from Wang et al. [56] thin-film phase map—one from each crystalline region—and use OptiMat Alloys with the MACE omat-0 calculator to predict bulk SQS properties. For each composition, the agent generates multiple independent SQS configurations in the experimentally observed structure type (54-atom cells for BCC and HCP) as well as in FCC (48-atom cells) for cross-structure comparison, relaxes the structures, and computes lattice parameters—all persisted automatically in the living database.

**BCC composition: 7.6Co–19.3Cr–8.4Fe–20.7Mo–9.1Ni–34.9W (at.%).** This W/Mo-rich composition corresponds to the region of highest hardness and elastic modulus in the thin-film library. The 54-atom SQS cells approximate the target composition to within  $\sim 1$  at.% (7.4Co–18.5Cr–9.3Fe–20.4Mo–9.3Ni–35.2W in at.%). Across 15 independent configurations, MACE predicts a BCC lattice parameter of  $a = 3.036 \pm 0.001$  Å at 0 K, increasing by  $\sim 0.58\%$  to  $3.054 \pm 0.001$  Å at room temperature (QHA). Wang et al. [56] report a range of  $a = 3.08$ – $3.11$  Å across the entire BCC region of the thin-film phase map [56], which spans a broad range of compositions; the predicted bulk value falls slightly below this range, suggesting that the BCC film is under tensile residual strain that expands the lattice relative to the stress-free bulk equilibrium. Additional contributions from finite temperature and porosity in the sputtered nanocrystalline film may further widen the gap. Comparing the Gibbs free energy of BCC and FCC structures as a function of temperature (Fig. 5a), BCC is thermodynamically preferred over FCC across the entire 0–600 K range, consistent with the experimentally observed BCC phase in this compositional region.

MACE elastic property calculations yield a bulk modulus  $K = 258 \pm 2$  GPa and a Hill Young’s modulus  $E_{VRH} = 236 \pm 5$  GPa,  $\sim 20\%$  higher than the thin-film nanoindentation value of  $199 \pm 8$  GPa reported by Wang et al. [56]; this discrepancy can be caused by the 4–8% porosity in sputtered nanocrystalline films, which significantly reduces the effective modulus relative to a defect-free bulk crystal. Thermal softening can also reduce the computed moduli at 0 K, e.g., the MACE bulk modulus at 300 K is around  $247 \pm 1$  GPa. Comparing the BCC six-component alloy with the FCC equiatom CoCrFeNi (Section 2.5.1), the BCC alloy has a much higher bulk modulus ( $K = 258$  vs. 173 GPa) and lower Zener anisotropy ( $A = 1.83$  vs. 2.97). For Young’s modulus, the Voigt and

Reuss bounds bracket the comparison differently due to the alloys’ contrasting anisotropy, but the Hill average places BCC modestly higher ( $E_H = 237$  vs. 225 GPa).

**HCP composition: 38Co–10.2Cr–15Fe–8.4Mo–21.3Ni–7.1W (at.%).** This Co/Ni-rich composition lies in the HCP region of the thin-film phase map. The 54-atom SQS cells approximate the target composition to within  $\sim 1$  at.% (e.g., 38.9Co–9.3Cr–14.8Fe–9.3Mo–20.4Ni–7.4W in at.%). With hydrostatic relaxation (preserving the ideal  $c/a = \sqrt{8/3} \approx 1.633$ ), MACE (15 configurations) predicts  $a = 2.543 \pm 0.002$  Å and  $c = 4.153 \pm 0.003$  Å at 0 K, increasing by  $\sim 0.45\%$  to  $a = 2.554 \pm 0.002$  Å and  $c = 4.171 \pm 0.003$  Å at room temperature (QHA). Across the entire HCP region, the thin-film XRD values span  $a = 2.510$ – $2.522$  Å and  $c = 4.128$ – $4.139$  Å [56]; the predicted bulk values fall above these ranges, suggesting that the HCP film is under compressive residual strain that contracts the lattice relative to the stress-free bulk equilibrium. The opposite strain states in the BCC and HCP films—tensile and compressive, respectively—are physically consistent with their markedly different compositions and growth modes under the same deposition conditions [56]. The QHA Gibbs free energy comparison (Fig. 5b) shows that FCC is consistently lower in energy than HCP across 0–600 K by  $\sim 3$  kJ/mol/atom, suggesting that FCC is the thermodynamically preferred phase for this composition in the bulk equilibrium limit. The experimental observation of HCP in the sputtered thin film [56] may therefore reflect non-equilibrium effects—residual stress, kinetic trapping during deposition, or chemical short-range ordering—that stabilize the HCP phase in the thin-film environment. Elastic calculations give  $K = 192 \pm 2$  GPa and  $E_{\text{VRH}} = 215 \pm 6$  GPa, with QHA thermal softening reducing  $K$  to  $186 \pm 2$  GPa at 300 K. Both moduli are lower than those of the BCC six-component alloy ( $K = 258$ ,  $E_{\text{VRH}} = 236$  GPa), consistent with the lower concentration of heavy refractory elements (Mo, W) in the Co/Ni-rich composition.

Together, these results provide bulk equilibrium predictions—lattice parameters, elastic moduli, and phase stability—that complement the thin-film measurements. The computational cost per composition is modest: with the MACE calculator on a consumer GPU, generating 15 independent SQS configurations of a 54-atom cell takes  $\sim 2$  min in total, computing elastic properties adds  $\sim 80$  min, and QHA thermal calculations require a further  $\sim 120$  min—approximately 3.5 h in total per composition. Scaling to hundreds of compositions is therefore feasible within days on a single GPU, enabling rapid pre-screening of bulk alloy properties across broad compositional libraries. By complementing experimental alloy screening and characterization with rich property prediction by OptiMat Alloys, experimental labs could significantly enhance the throughput and separate thin film deposition effects from true bulk properties of random alloys.

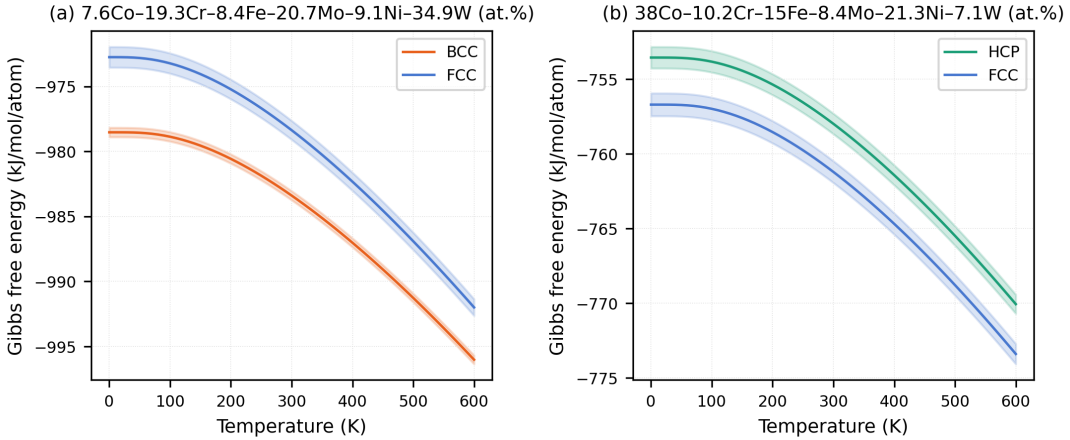


Figure 5: Gibbs free energy versus temperature for two compositions from Wang et al.’s thin-film library [56], computed via QHA with the MACE omat-0 calculator. (a) W/Mo-rich composition: BCC is clearly preferred over FCC at all temperatures. (b) Co/Ni-rich composition: FCC is consistently lower in energy than HCP by  $\sim 3$  kJ/mol/atom. Solid lines show the ensemble mean and shaded bands indicate  $\pm 1$  standard deviation over 15 independent SQS configurations.

### 2.5.3. Knowledge accumulation payoff

The calculations in Sections 2.5.1 and 2.5.2 were performed independently—CoCrFeNi as a validation baseline, the six-component alloys to explore Wang et al.’s thin-film compositions—yet the living database now contains a self-consistent dataset that enables comparisons neither user originally intended. For example, the effect of adding Mo and W to an equiatomic CoCrFeNi base alloy on elastic properties can be assessed immediately, without any additional computation, simply because both endpoints already reside in the database. This illustrates three features of the living-database paradigm. First, *the living database eliminates redundant computation*: the CoCrFeNi baseline was computed once and cached; any future user querying the same composition will retrieve the stored results without recomputation. Second, *knowledge accumulates through use*: as different users explore different compositions for their own purposes, the database organically builds coverage of the composition space without any centrally planned screening campaign. Third, *uncertainty quantification is organic*: repeated SQS configurations for the same composition yield ensemble statistics—all without bespoke convergence studies.

To demonstrate this concretely, we issue a single natural-language query: “Compare the elastic properties of BCC  $\text{Co}_4\text{Cr}_{10}\text{Fe}_5\text{Mo}_{11}\text{Ni}_5\text{W}_{19}$  and equiatomic CoCrFeNi computed using MACE calculator.” The agent searches the database, identifies matching entries for both compositions, averages over 10 cached SQS configurations each, and returns a side-by-side comparison of bulk modulus, shear modulus, Young’s modulus, Poisson’s ratio, Pugh ratio, and anisotropy index—together with scientific interpretation of the results (Fig. 6). No new calculations are triggered; the entire response is assembled from previously stored data. The scientific interpretation is generated by the underlying LLM’s reasoning capabilities. We find that the LLM reliably handles quantitative comparisons of the computed data—for example, the reported 48% increase in bulk modulus from FCC CoCrFeNi to BCC  $\text{Co}_4\text{Cr}_{10}\text{Fe}_5\text{Mo}_{11}\text{Ni}_5\text{W}_{19}$  is correct—but can produce internally inconsistent scientific interpretations—for example, drawing contradictory ductility conclusions from Poisson’s ratio and Pugh ratio despite both indicators pointing in the same direction. Such reasoning errors could be mitigated by integrating a retrieval-augmented generation (RAG) system that supplies domain-specific interpretations and guidance as context.

A traditional DFT workflow covering the same scope would require a few weeks of effort on a supercomputer; OptiMat Alloys compresses this to hours of GPU time per composition on a consumer workstation, with the caveat that the SQS approach does not capture chemical short-range order (CSRO), which can shift elastic constants by 5–15% [50]; integrating hybrid Monte Carlo/molecular dynamics methods to capture CSRO is planned for a future version of the agent [57].

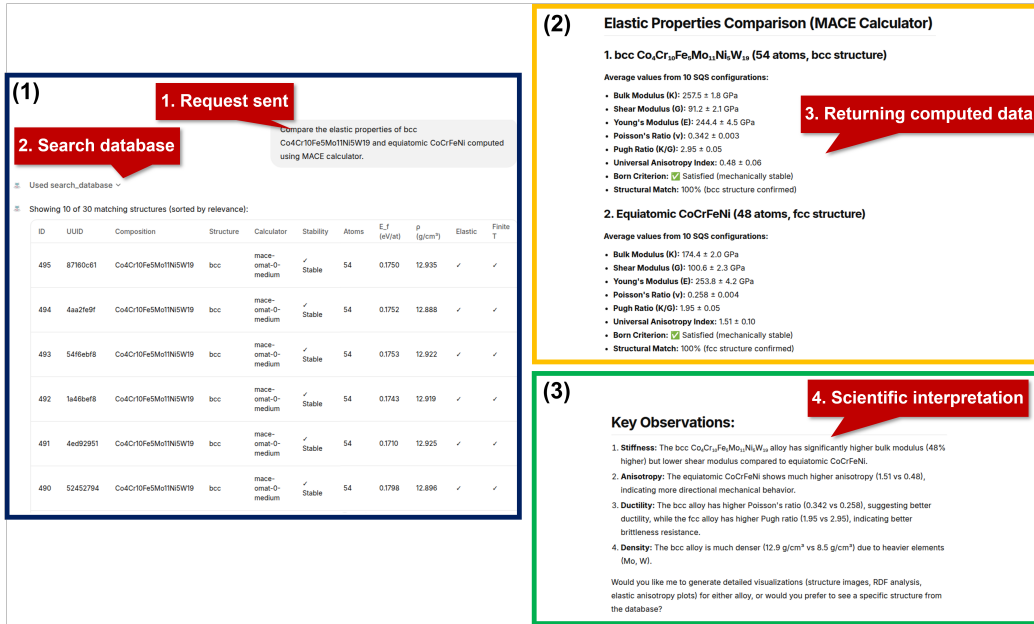


Figure 6: OptiMat Alloys interface demonstrating knowledge retrieval from the living database. The user issues a natural-language query requesting comparison of elastic properties between BCC Co<sub>4</sub>Cr<sub>10</sub>Fe<sub>5</sub>Mo<sub>11</sub>Ni<sub>5</sub>W<sub>19</sub> and equiatomic FCC CoCrFeNi. The agent (1) searches the database for matching entries, (2) retrieves and averages elastic properties over 10 cached SQS configurations per composition, and (3) provides scientific interpretation of the comparison—all without triggering new calculations.

### 3. Discussion

The preceding results demonstrate that OptiMat Alloys can screen alloy compositions with near-DFT fidelity, accumulate results in a persistent database, and remain accessible to users without programming expertise. Here we situate these capabilities within the broader challenge of scaling materials data infrastructure, using the four-V framework (Volume, Variety, Velocity, Veracity) of Scheffler et al. [2] to organize the discussion, before outlining open challenges for the emerging field of agentic computing in materials science.

Figure 7 maps each of the four dimensions to a specific contribution of OptiMat Alloys.

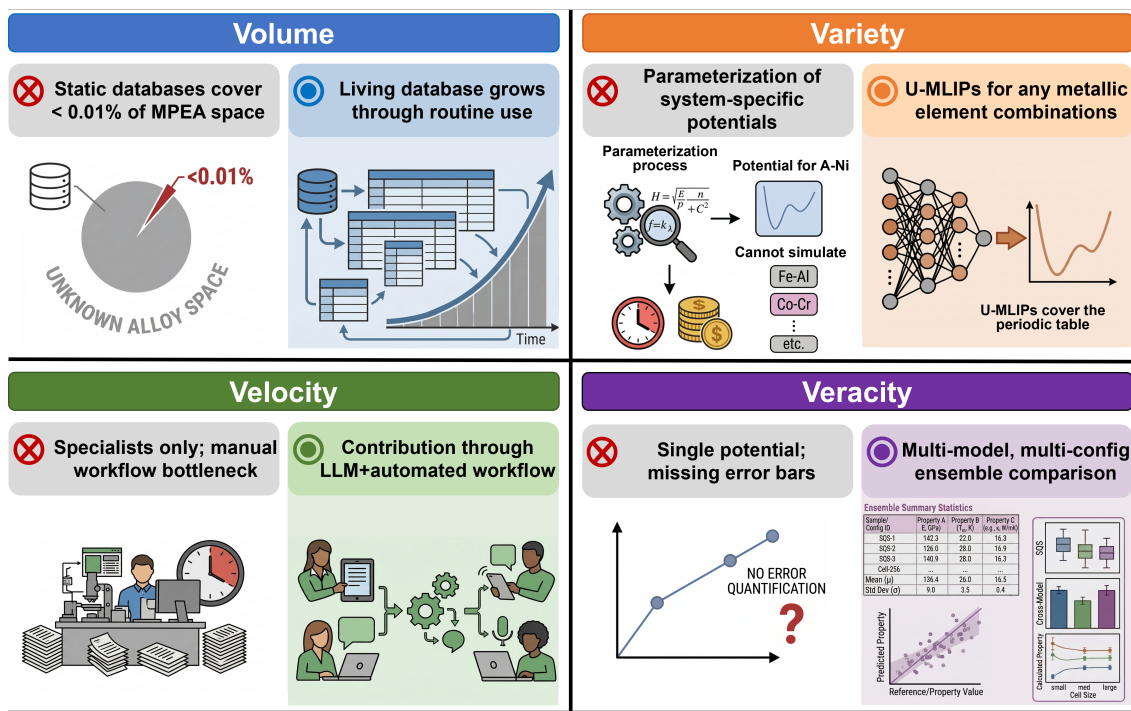


Figure 7: The four Vs of big data applied to computational alloy discovery. Each quadrant maps a current limitation of existing databases and agentic systems (left) to the corresponding OptiMat Alloys contribution (right). The framework addresses all four dimensions identified by Scheffler et al. [2] as limiting current materials data infrastructure.

- Volume.** Existing systems handle data in three ways: (i) static pre-computation (Materials Project, AFLOW, JARVIS), where only pre-computed entries can be queried; (ii) ephemeral on-demand computation (AtomAgents, MDAgent, QUASAR), where results are discarded after the session; and (iii) read-only retrieval (LLaMP, MatSciAgent, ChemCrow), where agents query databases but cannot contribute new data. All three leave a unidirectional data flow—database to user—rather than the bidirectional exchange needed to grow coverage. OptiMat Alloys introduces a mechanism that unifies computation and deposition: queries trigger calculations stored persistently with full provenance, so that asking a question *is* the FAIR data deposition event, removing both the expertise gate and the deliberate upload step. Because the agent enforces a single computational pipeline (standardized relaxation, elastic, and thermal protocols with a fixed output schema), every record is structurally and methodologically consistent by construction—eliminating the per-record curation bottleneck of traditional repositories. A cloud-hosted PostgreSQL component is under development to aggregate contributions across users, enabling structures computed by one researcher to benefit all others. Together, automated generation, full-data persistence, and built-in consistency grow database *volume* organically through use.
- Variety.** A critical but under-reported barrier in atomistic workflows is the availability of interatomic potentials. For quaternary and quinary MPEAs, classical parameterizations are largely nonexistent; even when a potential covers the required elemental combination, it is typically fitted to specific phenomena and may be unreliable outside that domain. Integrating a new potential—validating against known properties, configuring file formats, running benchmark calculations—adds significant overhead, a cost that recurs for every new elemental combination. Early LLM agents inherit this bottleneck: AtomAgents relies on EAM potentials [28], ToPolyAgent on Lennard-Jones/FENE [58], and MDAgent on LAMMPS force fields [30]. Recent systems have begun adopting universal ML force fields—LLaMP and Crystalyse use MACE-MP-0 [31, 59], LangSim supports MACE alongside EMT [60], and QUASAR integrates MACE within multi-scale workflows [32]. OptiMat Alloys integrates multiple universal potentials (ORB, NequIP, MACE), each trained on large-scale DFT datasets spanning

most of the periodic table, removing per-system parameterization entirely. By scoping to metallic systems—where these models reliably reproduce structural, thermodynamic, and mechanical properties (Supplementary Section S4.3)—the framework operates in the regime of highest accuracy, expanding the *variety* of systems accessible without manual intervention.

- **Velocity.** Two barriers throttle the rate at which new data can be generated: computational scientists face recurring manual overhead for every new composition (configuring inputs, launching simulations, parsing outputs), while experimentalists and other domain specialists—who possess the synthesis intuition to identify promising compositions—are excluded entirely because the interface to atomistic simulation has historically been code, not human language. LLMs address both simultaneously, parsing natural-language requests into structured tool calls that drive simulations autonomously [61, 62]. OptiMat Alloys treats the LLM as a swappable module via OpenRouter and Ollama integration; our evaluation of six backends (Supplementary Section S3) shows that free reasoning-capable models show superior ability in scientific tool-calling, suggesting that inference-time reasoning is the key factor for reliable agent orchestration. Local deployment via Ollama is functional for straightforward, single-turn queries but remains limited by context-window constraints on consumer hardware (Section 2.1). Complementing LLM automation, low-barrier deployment of the agent converts computational advances from niche capabilities into community-wide tools, expanding the contributor base from the estimated 5–15% with programming expertise to 85–95% including experimentalists and domain specialists. Higher *velocity* compounds directly into greater *volume* as each computation persists in the living database.
- **Veracity.** Surveyed agents that perform atomistic simulation rely on a single ML potential and a single atomic configuration, providing point estimates rather than confidence intervals [28, 30, 58]. OptiMat Alloys addresses this along two axes: *inter-model precision*, where any result can be recomputed with an alternative universal potential (ORB, MACE, NequIP) to quantify calculator dependence; and *configurational precision*, where repeated SQS queries accumulate an ensemble whose standard deviation captures sensitivity to atomic arrangement. These statistics emerge organically from the living database as each re-query adds a configuration. Several limitations bound this approach: inter-model spread quantifies precision, not accuracy—all potentials inherit systematic biases from PBE-GGA training data. The current workflow does not incorporate Monte Carlo methods for CSRO beyond the SQS random-alloy baseline. The framework is therefore a practical first filter that flags model disagreement and insufficient sampling, not a replacement for Bayesian uncertainty methods [63] or DFT validation of final-stage candidates.

Beyond these four dimensions, the rapid emergence of agentic systems raises broader challenges for the field. Rapid proliferation of agentic systems creates urgent challenges that the community must address. First, *reproducibility*: agent-mediated results depend on the ML potential, version, stochastic elements (SQS generation, temperature sampling), and—less critically for numerical outcomes but important for workflow fidelity—the LLM, which providers may update or deprecate without notice. Reproducing an agent’s result therefore requires pinning all three layers—a provenance chain more complex than traditional simulation workflows [9]. Containerization and provenance strategies adopted by several systems address parts of this challenge, but no standardized format yet captures this full dependency chain. Second, *validation standards*: no community-wide benchmarks exist for evaluating agent accuracy or reliability in the emerging agentic computing field. Each system validates against different test sets, making cross-system comparison difficult; standardized evaluation suites—analogue to Matbench Discovery for ML potentials [64]—would enable meaningful comparison. Third, *interoperability*: the 20 surveyed agents use different data formats, simulation backends, and persistence strategies, so without common data exchange protocols, results remain confined within individual agent ecosystems. Fourth, *community governance*: the open availability of 19/20 systems is commendable but insufficient alone. The field would benefit from shared registries of agents with documented capabilities, versioned provenance standards, and agreed-upon reporting requirements for agent-generated results.

The same community-driven, iterative approach that produced the FAIR data principles can guide development of responsible practices for agentic computing in materials science. The field advances not through a single tool serving all users, but through complementary systems spanning

the barrier–capability space—and community standards will be needed to ensure their collective output is trustworthy and interoperable.

## 4. Methods

### 4.1. Computational Framework

OptiMat Alloys integrates large language model agents with atomistic simulation capabilities through an AutoGen-based agentic framework [36] and the Atomic Simulation Environment (ASE) [19]. The framework supports interchangeable LLM backends; six models were evaluated on a 10-test tool-calling suite comprising seven standard operation tests and three error-handling tests, with GPT-OSS-120B [41] via Ollama Cloud [38] recommended as the default (Supplementary Section S3). The system supports eight universal machine-learning interatomic potentials (U-MLIPs) from three families: ORB [22], NequIP [23], and MACE [24]. All are trained on PBE-GGA density functional theory data with PAW pseudopotentials [65], drawn from three primary datasets—OMat24 [66] (100+ million configurations), MPtrj [67] (1.58 million trajectory frames), and sAlex [68]—so that the effective level of theory for metallic alloys is plain PBE without Hubbard corrections. Element coverage varies across families: ORB supports 117 of 118 elements, MACE 89, and NequIP 86 (Supplementary Section S4). ORB v3 serves as the default calculator, while NequIP oam-xl provides maximum accuracy and MACE omat-0-medium is optimized for phonon calculations (Supplementary Table S6). The agent orchestrates structure generation, relaxation, analysis, and property prediction via seven tool functions (Supplementary Table S14), while a living SQLite database records all structures and provenance.

### 4.2. Structure Generation and Relaxation

Chemically disordered alloys are modeled using special quasirandom structures (SQS) [69, 70] generated via Monte Carlo optimization that minimizes the objective function  $\Phi = \sum_s w_s (\Pi_{\text{actual}}(s) - \Pi_{\text{random}}(s))^2$ , where  $\Pi(s)$  is the pair correlation for neighbor shell  $s$  and  $w_s$  are shell weights ( $w_1 = 1.0$ ,  $w_2 = 0.5$ ;  $10^7$  Monte Carlo iterations). Because the optimization is stochastic, each generation produces a distinct atomic arrangement even for the same composition and structure type. Initial lattice constants are estimated via Vegard’s law [71],  $a_{\text{alloy}} = \sum_i x_i \cdot a_i$ , using reference values precomputed for each calculator by relaxing all 118 elements in five structure types (SC, BCC, FCC, HCP, diamond). Unit cells are replicated to create supercells with target atom counts (typically 500–2000 atoms) while preserving requested compositions.

Relaxation follows a two-stage FIRE [72] protocol. Stage 1 runs on GPU with convergence threshold  $f_{\text{max}} = 0.01$  eV/Å (max 500 steps) for rapid removal of large forces and volume equilibration. Stage 2 switches to CPU with  $f_{\text{max}} = 0.001$  eV/Å (max 500 steps) to achieve tight convergence while avoiding GPU numerical noise. Both stages use ASE’s [19] `FrechetCellFilter` with `hydrostatic_strain=True`, which maps cell strain components to virtual atomic coordinates so that FIRE can simultaneously optimize cell volume and atomic positions while preserving cell shape. The cell shape constraint is intentional: without it, the optimizer may transform the structure to a different phase (e.g., FCC  $\rightarrow$  HCP), preventing systematic cross-composition comparison within a consistent crystallographic framework (Supplementary Methods S3.1).

### 4.3. Property Calculations

Formation energies are computed relative to single-element references using ground-state structures. Structural analysis employs PTM [73] for phase identification and radial distribution functions (RDF) for coordination characterization.

Elastic stiffness tensors are obtained via the finite-difference strain–energy method. The deformation set comprises 180 asymmetric strain states: 45 unique index pairs from the  $3 \times 3$  strain tensor (with replacement)  $\times$  4 sign combinations ( $\pm\delta, \pm\delta$ ) at magnitude  $\delta = 0.01$  (1%). For each deformation, the strained cell  $\mathbf{h}_{\text{strained}} = \mathbf{h}_0 \cdot (\mathbf{I} + \boldsymbol{\epsilon})$  is constructed, atomic positions are relaxed at fixed cell (FIRE,  $f_{\text{max}} = 0.005$  eV/Å, max 100 steps), and the total energy is

recorded. The symmetric  $C_{ijkl}$  tensor is recovered via least-squares fitting of the quadratic energy-strain relationship  $E(\boldsymbol{\epsilon}) = E_0 + \frac{V_0}{2} \sum_{ijkl} C_{ijkl} \epsilon_{ij} \epsilon_{kl}$ , using a design matrix  $M_{n,ijkl} = \frac{1}{2} \epsilon_{ij}^{(n)} \epsilon_{kl}^{(n)}$  and solving  $\mathbf{C} = (\mathbf{M}^T \mathbf{M})^{-1} \mathbf{M}^T \mathbf{E}$ . Polycrystalline bulk ( $K$ ) and shear ( $G$ ) moduli are computed via Voigt–Reuss–Hill averaging [74], with Young’s modulus  $E = 9KG/(3K + G)$  and Poisson’s ratio  $\nu = (3K - 2G)/(6K + 2G)$  from isotropic relations. The Pugh ratio [75]  $K/G$  serves as a ductility indicator ( $K/G > 1.75$ : ductile), and the universal elastic anisotropy index  $A^U = 5G_V/G_R + K_V/K_R - 6$  [76] quantifies deviation from isotropy. Directional single-crystal properties are computed from the compliance tensor via ELATE [77], and mechanical stability is validated against the Born criteria [78, 79] for the appropriate symmetry class (Supplementary Methods S3.3). Elastic property calculations require 20–60 min depending on system size.

Temperature-dependent thermodynamic properties are computed using the quasi-harmonic approximation (QHA) [80] via phonopy [81]. Phonon calculations are performed at 11 volumes spanning  $\pm 10\%$  strain around the 0 K equilibrium volume ( $V_i = V_0 \times \{0.90, 0.92, \dots, 1.10\}$ ). At each volume, the structure is scaled isotropically, atomic positions are relaxed at fixed cell (FIRE,  $f_{\max} = 0.01$  eV/Å, max 100 steps), and force constants are obtained via finite differences from phonopy displacement configurations. The phonon density of states is computed on a  $20 \times 20 \times 20$   $q$ -point mesh, yielding the Helmholtz free energy  $F(V, T) = E_{\text{static}}(V) + F_{\text{vib}}(V, T)$  over the temperature range 0–600 K. At each temperature,  $F(V, T)$  is fitted to the Vinet equation of state [82], and thermodynamic properties are obtained as derivatives of the Gibbs free energy  $G(T, P) = \min_V [F(V, T) + PV]$ : thermal expansion  $\alpha(T)$ , bulk modulus  $B(T)$ , and isobaric heat capacity  $C_p(T) = C_V + \alpha^2 BVT$ , where the Grüneisen parameter  $\gamma = \alpha BV/C_V$  characterizes anharmonicity (Supplementary Methods S3.4). QHA calculations require 1–4 h per composition. Each structure generates a comprehensive report including OVITO [35]-rendered visualizations, property tables, and exportable data files (CIF, POSCAR, CSV) with full bibliography (Supplementary Section S6.2). Critically, each report also records the computational methods, parameters, and calculator version used, providing a self-contained reproducibility record that allows any result to be independently verified or recomputed.

#### 4.4. Data Management and Cross-Potential Validation

Each structure receives a UUID4 identifier—a 128-bit random hexadecimal string drawn from a namespace of  $2^{122}$  values—with dedicated storage for images, trajectories, and computed properties (Supplementary Section S6.1). UUID4 was chosen deliberately for its decentralized properties: any researcher running an independent local instance generates identifiers that are virtually guaranteed to be collision-free ( $p < 10^{-18}$  even at one billion entries), so databases from separate groups can be merged into a shared repository without requiring a central authority or identifier registry.

The SQLite database uses ASE’s key–value store, which supports scalar types (string, integer, float, boolean) for indexed queries. Searchable fields include the UUID, calculator name, composition string, target structure (sc, bcc, fcc, hcp, diamond), number of atoms, per-element atomic fractions, potential energy, formation energy (ground-state reference), mixing energy (same-structure reference), mass density, lattice constant, PTM match percentage, and a boolean `is_structurally_stable` flag (true when PTM match  $\geq 90\%$ ). When QHA data is present, representative 300 K scalars (Gibbs free energy, bulk modulus, isobaric heat capacity, thermal expansion, Grüneisen parameter) are also stored as searchable fields alongside `has_qha_data` and `qha_dynamically_stable` flags. Array-valued and nested results that cannot be represented as scalars—including RDF arrays, the full  $6 \times 6$  stiffness tensor with Voigt/Reuss/Hill moduli, ELATE directional properties, Born stability eigenvalues, and 2D QHA grids  $F(T, V)$ ,  $S(T, V)$ ,  $C_V(T, V)$  with their derived 1D curves—are stored in a JSON data blob attached to each entry. Provenance fields (calculator identity, `derived_from` link, and ISO 8601 creation/modification timestamps) support reproducibility and enable tracing recomputed structures back to their source. Before computing a new structure, the agent queries the database for matching composition (within tolerance), structure type, and atom count; cache hits return existing results while misses trigger new calculations that are stored for future queries (Supplementary Section S6.5).

Cross-potential validation is supported through a dedicated `recompute_structure` tool that enables systematic comparison of U-MLIPs on identical input configurations. Given a source structure reference (integer ID or UUID), the tool (1) loads the stored relaxed atoms (positions, cell,

and composition) from the database, (2) switches to the target U-MLIP (e.g., NequIP oam-xl in place of ORB v3), (3) applies the same two-stage FIRE relaxation protocol (Stage 1 on CUDA with  $f_{\max} = 0.01$  eV/Å; Stage 2 on CPU with  $f_{\max}$  configurable, default 0.001 eV/Å) starting from the source relaxed structure, (4) recomputes potential energy, formation energy and mixing energy (using the target calculator’s precomputed reference data), density, lattice constant, stress tensor, PTM structural analysis, and structural stability assessment, and (5) stores the result as a new database entry with a `derived_from` link to the source UUID and a `recomputed_from_calculator` field recording the source calculator. The tool returns an explicit pairwise comparison between source and new calculator—differences in potential energy, formation energy, density, and PTM match percentage—so that calculator-specific deviations can be assessed directly without manual post-processing. By fixing the input configuration, this workflow isolates calculator-specific differences in final relaxed geometry, energetics, and structural stability from the variations that would otherwise arise from independent SQS realizations, enabling controlled benchmarking across ORB, NequIP, and MACE as well as multi-calculator consensus for high-throughput screening (Supplementary Section S6.3).

## Supplementary Information

This Supplementary Information (SI) provides additional details on the thermodynamic and experimental databases underpinning the combinatorial space analysis (Section S1), the agent prompts and tool annotations (Section S2), the LLM backbone evaluation (Section S3), supported calculators and their validation against DFT and experiment (Section S4), computational methods for relaxation, SQS generation, elastic tensors, and quasi-harmonic properties (Section S5), and the system architecture including database schema, agent tools, and deployment comparison (Section S6).

## References

- [1] Mark D. Wilkinson, Michel Dumontier, IJsbrand Jan Aalbersberg, Gabrielle Appleton, Myles Axton, Arie Baak, Niklas Blomberg, Jan-Willem Boiten, Luiz Bonino da Silva Santos, Philip E. Bourne, Jildau Bouwman, Anthony J. Brookes, Tim Clark, Mercè Crosas, Ingrid Dillo, Olivier Dumon, Scott Edmunds, Chris T. Evelo, Richard Finkers, Alejandra Gonzalez-Beltran, Alasdair J.G. Gray, Paul Groth, Carole Goble, Jeffrey S. Grethe, Jaap Heringa, Peter A.C ’t Hoen, Rob Hooft, Tobias Kuhn, Ruben Kok, Joost Kok, Scott J. Lusher, Maryann E. Martone, Albert Mons, Abel L. Packer, Bengt Persson, Philippe Rocca-Serra, Marco Roos, Rene van Schaik, Susanna-Assunta Sansone, Erik Schultes, Thierry Sengstag, Ted Slater, George Strawn, Morris A. Swertz, Mark Thompson, Johan van der Lei, Erik van Mulligen, Jan Velterop, Andra Waagmeester, Peter Wittenburg, Katherine Wolstencroft, Jun Zhao, and Barend Mons. The fair guiding principles for scientific data management and stewardship. *Scientific Data*, 3:160018, 2016. Published March 15, 2016.
- [2] Matthias Scheffler, Martin Aeschlimann, Martin Albrecht, Tristan Berau, Hans-Joachim Bungartz, Claudia Felser, Mark Greiner, Axel Groß, Christoph T. Koch, Kurt Kremer, Wolfgang A. Nagel, Taisuke Nakamura, Kikuji Sagiyama, Alexander Schlüter, Georg Spenke, Dagmar Stachel, Christoph Strunk, Thomas Weidinger, et al. Fair data enabling new horizons for materials research. *Nature*, 604:635–642, 2022. Review connecting FAIR data principles to materials science advances.
- [3] Claudia Draxl and Matthias Scheffler. The NOMAD laboratory: from data sharing to artificial intelligence. *Journal of Physics: Materials*, 2(3):036001, 2019. NOMAD repository and AI toolkit.
- [4] Anubhav Jain, Shyue Ping Ong, Geoffroy Hautier, Wei Chen, William Davidson Richards, Stephen Dacek, Shreyas Cholia, Dan Gunter, David Skinner, Gerbrand Ceder, and Kristin A. Persson. Commentary: The materials project: A materials genome approach to accelerating materials innovation. *APL Materials*, 1(1):011002, 2013.

- [5] Matthew K. Horton, Patrick Huck, Ruo Xi Yang, Jason M. Munro, Shyam Dwaraknath, Alex M. Ganose, Ryan S. Kingsbury, Mingjian Wen, Jimmy X. Shen, Tyler S. Mathis, Aaron D. Kaplan, Karlo Berket, Janosh Riebesell, Janine George, Andrew S. Rosen, Evan W. C. Spottesmith, Matthew J. McDermott, Orion A. Cohen, Alex Dunn, Matthew C. Kuner, Gian-Marco Rignanese, Guido Petretto, David Waroquiers, Sinead M. Griffin, Jeffrey B. Neaton, Daryl C. Chrzan, Mark Asta, Geoffroy Hautier, Shreyas Cholia, Gerbrand Ceder, Shyue Ping Ong, Anubhav Jain, and Kristin A. Persson. Accelerated data-driven materials science with the Materials Project. *Nature Materials*, 24:1522–1532, 2025.
- [6] Stefano Curtarolo, Wahyu Setyawan, Gus L. W. Hart, Michal Jahnatek, Roman V. Chepulskii, Richard H. Taylor, Shidong Wang, Junkai Xue, Kesong Yang, Ohad Levy, Michael J. Mehl, Harold T. Stokes, Denis O. Demchenko, and Dane Morgan. Aflow: An automatic framework for high-throughput materials discovery. *Computational Materials Science*, 58:218–226, 2012.
- [7] Kamal Choudhary, Kevin F. Garrity, Andrew C. E. Reid, Brian DeCost, Adam J. Biacchi, Angela R. Hight Walker, Zachary Trautt, Jason Hattrick-Simpers, A. Gilad Kusne, Andrea Centrone, Albert Davydov, Jie Jiang, Ruth Pachter, Anne Chaka, and Francesca Tavazza. The joint automated repository for various integrated simulations (JARVIS) for data-driven materials design. *npj Computational Materials*, 6:173, 2020.
- [8] Leopold Talirz, Snehal Kumbhar, Elsa Passaro, Aliaksandr V. Yakutovich, Valeria Granata, Fernando Gargiulo, Marco Borelli, Martin Uhrin, Sebastiaan P. Huber, Spyros Zoupanos, Carl S. Adorf, Casper W. Andersen, Ole Schütt, Carlo A. Pignedoli, Daniele Passerone, Joost VandeVondele, Thomas C. Schulthess, Berend Smit, Giovanni Pizzi, and Nicola Marzari. Materials cloud, a platform for open computational science. *Scientific Data*, 7(1):299, 2020.
- [9] Sebastiaan P. Huber, Spyros Zoupanos, Martin Uhrin, Leopold Talirz, Leonid Kahle, Rico Häuselmann, Dominik Gresch, Tiziano Müller, Aliaksandr V. Yakutovich, Casper W. Andersen, Francisco F. Ramirez, Carl S. Adorf, Fernando Gargiulo, Snehal Kumbhar, Elsa Passaro, Conrad Johnston, Andrius Merkys, Andrea Cepellotti, Nicolas Mounet, Nicola Marzari, Boris Kozinsky, and Giovanni Pizzi. Aiida 1.0, a scalable computational infrastructure for automated reproducible workflows and data provenance. *Scientific Data*, 7(1):300, 2020.
- [10] Patrick Huck, Daniel Gunter, Shreyas Cholia, Donald Winston, Alpha T. N’Diaye, and Kristin Persson. User applications driven by the community contribution framework MPContribs in the Materials Project. *Concurrency and Computation: Practice and Experience*, 28(7):1982–1993, 2016.
- [11] Easo P. George, Dierk Raabe, and Robert O. Ritchie. High-entropy alloys. *Nature Reviews Materials*, 4:515–534, 2019.
- [12] D. B. Miracle and O. N. Senkov. A critical review of high entropy alloys and related concepts. *Acta Materialia*, 122:448–511, 2017.
- [13] Thermo-Calc Software AB. Thermo-calc databases overview, 2025. Accessed: October 2025.
- [14] J. M. Rickman, H. M. Chan, M. P. Harmer, J. A. Smeltzer, C. J. Marvel, A. Roy, and G. Balasubramanian. Materials informatics for the screening of multi-principal elements and high-entropy alloys. *Nature Communications*, 10:2618, 2019. Quantifies the informatics challenge of screening MPEAs.
- [15] Ge Lei, R. Docherty, and Samuel J. Cooper. Materials science in the era of large language models: a perspective. *Digital Discovery*, 2024.
- [16] Lei Wang, Chen Ma, Xueyang Feng, Zeyu Zhang, Hao Yang, Jingsen Zhang, Zhiyuan Chen, Jiakai Tang, Xu Chen, Yankai Lin, Wayne Xin Zhao, Zhewei Wei, and Ji-Rong Wen. A survey on large language model based autonomous agents. *Frontiers of Computer Science*, 18:186345, 2024.
- [17] G. Kresse and J. Furthmüller. Efficient iterative schemes for ab initio total-energy calculations using a plane-wave basis set. *Physical Review B*, 54(16):11169–11186, 1996.

- [18] Aidan P. Thompson, H. Metin Aktulga, Richard Berger, Dan S. Bolintineanu, W. Michael Brown, Paul S. Crozier, Pieter J. in 't Veld, Axel Kohlmeyer, Stan G. Moore, Trung Dac Nguyen, Ray Shan, Mark J. Stevens, Julien Tranchida, Christian Trott, and Steven J. Plimpton. LAMMPS – a flexible simulation tool for particle-based materials modeling at the atomic, meso, and continuum scales. *Computer Physics Communications*, 271:108171, 2022.
- [19] Ask Hjorth Larsen, Jens Jørgen Mortensen, Jakob Blomqvist, Ivano E. Castelli, Rune Christensen, Marcin Dułak, Jesper Friis, Michael N. Groves, Bjørk Hammer, Cory Hargus, Eric D. Hermes, Paul C. Jennings, Peter Bjerre Jensen, James Kermode, John R. Kitchin, Esben Leonhard Kolsbjerg, Joseph Kubal, Kristen Kaasbjerg, Steen Lysgaard, Jón Bergmann Maronsson, Tristan Maxson, Thomas Olsen, Lars Pastewka, Andrew Peterson, Carsten Rostgaard, Jakob Schiøtz, Ole Schütt, Mikkel Strange, Kristian S. Thygesen, Tejs Vegge, Lasse Vilhelmsen, Michael Walter, Zhenhua Zeng, and Karsten W. Jacobsen. The atomic simulation environment—a python library for working with atoms. *Journal of Physics: Condensed Matter*, 29(27):273002, 2017.
- [20] Andrej Karpathy. Software 2.0. Medium, 2017. Defines Software 1.0 (classical code) vs 2.0 (neural networks).
- [21] Andrej Karpathy. Software is changing (again). Keynote at YC AI Startup School, San Francisco, June 2025, 2025. Extends Software 1.0/2.0 framework to Software 3.0 (LLMs as natural-language programming).
- [22] Albert Neumeier, Muhammed Shuaibi, Stephan Broderick, Florian Pokorny, et al. Orb: A fast, scalable neural network potential. arXiv preprint arXiv:2410.22570, 2024. Orbital Materials universal ML potential; also available at <https://github.com/orbital-materials/orb-models>.
- [23] Simon Batzner, Albert Musaelian, Lixin Sun, Mario Geiger, Jonathan P. Mailoa, Mordechai Kornbluth, Nicola Molinari, Tess E. Smidt, and Boris Kozinsky. E(3)-equivariant graph neural networks for data-efficient and accurate interatomic potentials. *Nature Communications*, 13:2453, 2022. NequIP architecture.
- [24] Ilyes Batatia, Dávid Péter Kovács, Gregor N. C. Simm, Christoph Ortner, and Gábor Csányi. Mace: Higher order equivariant message passing neural networks for fast and accurate force fields. *Advances in Neural Information Processing Systems*, 35:11423–11436, 2022. NeurIPS 2022.
- [25] Michelle Barker, Neil P. Chue Hong, Daniel S. Katz, Anna-Lena Lamprecht, Carlos Martinez-Ortiz, Fotis Psomopoulos, Jennifer Harber, Leyla Jael Castro, Martin Gruber, Paula Grenier, et al. Introducing the FAIR principles for research software. *Scientific Data*, 9:622, 2022. FAIR4RS: extends FAIR from data to research software.
- [26] Daniil A. Boiko, Robert MacKnight, Ben Kline, and Gabe Gomes. Autonomous chemical research with large language models. *Nature*, 624:570–578, 2023. Coscientist system.
- [27] Andres M. Bran, Sam Cox, Oliver Schilter, Carlo Baldassari, Andrew D. White, and Philippe Schwaller. Augmenting large language models with chemistry tools. *Nature Machine Intelligence*, 6:525–535, 2024. ChemCrow system.
- [28] Alireza Ghafarollahi and Markus J. Buehler. Automating alloy design and discovery with physics-aware multimodal multiagent ai. *Proceedings of the National Academy of Sciences*, 122(7):e2414074122, 2025. AtomAgents system; published January 2025.
- [29] Akshat Chaudhari, Janghoon Ock, and Amir Barati Farimani. Modular large language model agents for multi-task computational materials science. ChemRxiv preprint, 2025. MatSciAgent system.
- [30] Zhuofan Shi, Chunxiao Xin, Tong Huo, Yuntao Jiang, Bowen Wu, Xingyue Chen, Wei Qin, Xinjian Ma, Gang Huang, Zhenyu Wang, and Xiang Jing. A fine-tuned large language model based molecular dynamics agent for code generation to obtain material thermodynamic parameters. *Scientific Reports*, 15:10295, 2025. MDAgent system.

- [31] Yuan Chiang, Chia-Hong Chou, and Janosh Riebesell. LLaMP: Large language model made powerful for high-fidelity materials knowledge retrieval and distillation. arXiv preprint arXiv:2401.17244, 2024. LLaMP system; also published at EMNLP 2025.
- [32] Fengxu Yang and Jack D. Evans. QUASAR: A universal autonomous system for atomistic simulation and a benchmark of its capabilities. arXiv preprint arXiv:2602.00185, 2026. QUASAR system.
- [33] Chainlit Team. Chainlit: Build production-ready conversational ai. <https://github.com/Chainlit/chainlit>, 2024. Accessed: 2025-11-22.
- [34] Nicolas Kruchten, Andrew Seier, and Chris Parmer. Plotly: An interactive, open-source, and browser-based graphing library for Python, 2026. Version 6.7.0. <https://github.com/plotly/plotly.py>.
- [35] Alexander Stukowski. Visualization and analysis of atomistic simulation data with ovito—the open visualization tool. *Modelling and Simulation in Materials Science and Engineering*, 18:015012, 2010. OVITO visualization software.
- [36] Qingyun Wu, Gagan Bansal, Jieyu Zhang, Yiran Wu, Beibin Li, Erkang Zhu, Li Jiang, Xiaoyun Zhang, Shaokun Zhang, Jiale Liu, et al. Autogen: Enabling next-gen llm applications via multi-agent conversations. In *First conference on language modeling*, 2024.
- [37] OpenRouter. OpenRouter: A unified interface for large language models, 2023. Accessed: April 2026.
- [38] Ollama Contributors. Ollama: Get up and running with large language models locally, 2023. Accessed: April 2026.
- [39] GLM Team. GLM-4.5: Agentic, reasoning, and coding (ARC) foundation models. arXiv preprint arXiv:2508.06471, 2025.
- [40] Xiaomi LLM-Core Team. MiMo-V2-Flash technical report. arXiv preprint arXiv:2601.02780, 2026.
- [41] OpenAI. gpt-oss-120b & gpt-oss-20b model card. arXiv preprint arXiv:2508.10925, 2025.
- [42] OpenAI. Introducing GPT-4.1 in the API. <https://openai.com/index/gpt-4-1/>, 2025. Accessed: 2026-02-05.
- [43] Nelson F. Liu, Kevin Lin, John Hewitt, Ashwin Paranjape, Michele Bevilacqua, Fabio Petroni, and Percy Liang. Lost in the middle: How language models use long contexts. *Transactions of the Association for Computational Linguistics*, 12:157–173, 2024.
- [44] Gene Simmons and Herbert Wang. *Single Crystal Elastic Constants and Calculated Aggregate Properties: A Handbook*. MIT Press, Cambridge, MA, 2nd edition, 1971.
- [45] Y. S. Touloukian, R. K. Kirby, R. E. Taylor, and P. D. Desai. *Thermophysical Properties of Matter, Vol. 12: Thermal Expansion—Metallic Elements and Alloys*. IFI/Plenum, New York, 1975.
- [46] Malcolm W. Chase, Jr. *NIST-JANAF Thermochemical Tables*. American Chemical Society and American Institute of Physics, 4th edition, 1998. Journal of Physical and Chemical Reference Data, Monograph No. 9.
- [47] Z. Wu, H. Bei, G. M. Pharr, and E. P. George. Temperature dependence of the mechanical properties of equiatomic solid solution alloys with face-centered cubic crystal structures. *Acta Materialia*, 81:428–441, 2014.
- [48] Ke Jin, B. C. Sales, G. M. Stocks, German Samolyuk, Markus Daene, W. J. Weber, Yanwen Zhang, and Hongbin Bei. Tailoring the physical properties of Ni-based single-phase equiatomic alloys by modifying the chemical complexity. *Scientific Reports*, 6:20159, 2016.

- [49] Natalia E. Koval, J. I. Juaristi, R. Díez Muiño, and M. Alducin. Structure and properties of CoCrFeNiX multi-principal element alloys from *ab initio* calculations. *Journal of Applied Physics*, 127(14):145102, 2020.
- [50] Mashroor S. Nitol, Artur Tamm, Subah Mubassira, Shuozhi Xu, and Saryu J. Fensin. Achieving DFT accuracy in short range ordering and stacking fault energy using moment tensor potential for CoCrFeNi and CoCrNi. arXiv preprint arXiv:2509.11231, 2025.
- [51] A. Tamm, A. Aabloo, M. Klintonberg, M. Stocks, and A. Caro. Atomic-scale properties of Ni-based FCC ternary, and quaternary alloys. *Acta Materialia*, 99:307–312, 2015.
- [52] A. J. Zaddach, Changning Niu, C. C. Koch, and Douglas L. Irving. Mechanical properties and stacking fault energies of NiFeCrCoMn high-entropy alloy. *JOM*, 65(12):1780–1789, 2013.
- [53] P. Nagy, N. Rohbeck, R. N. Widmer, Z. Hegedűs, J. Michler, L. Pethő, J. L. Lábár, and J. Gubicza. Combinatorial study of phase composition, microstructure and mechanical behavior of Co-Cr-Fe-Ni nanocrystalline film processed by multiple-beam-sputtering physical vapor deposition. *Materials*, 15(7):2319, 2022.
- [54] Giacomo Lorenzin, Fedor F Klimashin, Jeyun Yeom, Yang Hu, Johann Michler, Jolanta Janczak-Rusch, Vladyslav Turlo, and Claudia Cancellieri. Effect of residual stress and microstructure on mechanical properties of sputter-grown cu/w nanomultilayers. *APL Materials*, 12(10), 2024.
- [55] V. A. Bykov, T. V. Kulikova, I. S. Sipatov, E. V. Sterkhov, D. A. Kovalenko, and R. E. Ryltsev. Transport properties of equiatomic CoCrFeNi high-entropy alloy with a single-phase face-centered cubic structure. *Crystals*, 13(11):1567, 2023.
- [56] Ao Wang, László Pethő, Zoltán Hegedűs, Maria Watroba, Johann Michler, Jozef Veselý, Peter Minárik, Péter Nagy, and Jenő Gubicza. High-entropy alloy mapping in the Co-Cr-Fe-Mo-Ni-W compositional library using a combinatorial thin film. *Journal of Alloys and Compounds*, 1048:185264, 2025.
- [57] Babak Sadigh, Paul Erhart, Alexander Stukowski, Alfredo Caro, Enrique Martinez, and Luis Zepeda-Ruiz. Scalable parallel monte carlo algorithm for atomistic simulations of precipitation in alloys. *Physical Review B—Condensed Matter and Materials Physics*, 85(18):184203, 2012.
- [58] Lijie Ding, Jan-Michael Y. Carrillo, and Changwoo Do. ToPolyAgent: AI agents for coarse-grained topological polymer simulations. *Digital Discovery*, 2025. Also arXiv:2510.12091.
- [59] Ryan Nduma, Hyunsoo Park, and Aron Walsh. Crystalyse: a multi-tool agent for materials design. arXiv preprint arXiv:2512.00977, 2025.
- [60] Jan Janssen, Edward O. Pyzer-Knapp, Alex M. Ganose, et al. LangSim: Large language model interface for atomistic simulation. 2024 LLM Hackathon for Applications in Materials Science and Chemistry, 2024. Hackathon proceedings: arXiv:2411.15221.
- [61] Honghao Zhang, Yabo Li, Wenqian Huang, et al. Towards agentic intelligence for materials science. *arXiv preprint arXiv:2602.00169v2*, 2026.
- [62] Cheng Li, Ningxin Ran, and Jian Liu. Agentic material science. *Journal of Materials Informatics*, 6:10, 2026.
- [63] Félix Musil, Michael J. Willatt, Mikhail A. Langovoy, and Michele Ceriotti. Fast and accurate uncertainty estimation in chemical machine learning. *Journal of Chemical Theory and Computation*, 15(2):906–915, 2019.
- [64] Janosh Riebesell, Rhys E. A. Goodall, Philipp Benber, Yuan Chiang, Bowen Deng, Alpha A. Lee, Anubhav Jain, and Kristin A. Persson. Matbench discovery – a framework to evaluate machine learning crystal stability predictions. *arXiv preprint arXiv:2308.14920*, 2024. Matbench Discovery benchmark for ML potentials.

- [65] John P. Perdew, Kieron Burke, and Matthias Ernzerhof. Generalized gradient approximation made simple. *Physical Review Letters*, 77:3865–3868, 1996.
- [66] Luis Barroso-Luque, Shuaibi Muhammed, Xingang Xie, et al. Open materials 2024 (omat24) inorganic materials dataset and models. arXiv preprint arXiv:2410.12771, 2024. Meta FAIR dataset with 100M+ DFT calculations.
- [67] Bowen Deng, Peichen Zhong, KyuJung Jun, Janosh Riebesell, Kevin Han, Christopher J. Bartel, and Gerbrand Ceder. CHGNet as a pretrained universal neural network potential for charge-informed atomistic modelling. *Nature Machine Intelligence*, 5:1031–1041, 2023. Introduces the MPtrj dataset of 1.58M Materials Project trajectory frames.
- [68] Thibault Cavignac, Cong Gao, Jonathan Schmidt, Silvana Botti, and Miguel A. L. Marques. AI-driven expansion and application of the Alexandria database. arXiv preprint arXiv:2512.09169, 2024. Alexandria PBE dataset with MP-compatible settings.
- [69] Alex Zunger, S.-H. Wei, L. G. Ferreira, and James E. Bernard. Special quasirandom structures. *Physical Review Letters*, 65:353, 1990. Original SQS methodology.
- [70] Dominik Gehringer, Martin Friák, and David Holec. Models of configurationally-complex alloys made simple. *Computer Physics Communications*, 286:108664, 2023. sqsgenerator library.
- [71] L. Vegard. Die Konstitution der Mischkristalle und die Raumfüllung der Atome. *Zeitschrift für Physik*, 5(1):17–26, 1921.
- [72] Erik Bitzek, Pekka Koskinen, Franz Gähler, Michael Moseler, and Peter Gumbsch. Structural relaxation made simple. *Physical Review Letters*, 97:170201, 2006. FIRE (Fast Inertial Relaxation Engine) optimizer.
- [73] Peter Mahler Larsen, Søren Schmidt, and Jakob Schiøtz. Robust structural identification via polyhedral template matching. *Modelling and Simulation in Materials Science and Engineering*, 24:055007, 2016. Polyhedral Template Matching (PTM) algorithm.
- [74] R. Hill. The elastic behaviour of a crystalline aggregate. *Proceedings of the Physical Society. Section A*, 65:349–354, 1952. Hill averaging (arithmetic mean of Voigt and Reuss).
- [75] S. F. Pugh. XCII. relations between the elastic moduli and the plastic properties of polycrystalline pure metals. *The London, Edinburgh, and Dublin Philosophical Magazine and Journal of Science*, 45(367):823–843, 1954.
- [76] Shivakumar I. Ranganathan and Martin Ostoja-Starzewski. Universal elastic anisotropy index. *Physical Review Letters*, 101:055504, 2008. Universal anisotropy index  $A^U$ .
- [77] Romain Gaillac, Pluton Pullumbi, and François-Xavier Coudert. Elate: an open-source online application for analysis and visualization of elastic tensors. *Journal of Physics: Condensed Matter*, 28:275201, 2016. ELATE elastic anisotropy visualization.
- [78] Max Born and Kun Huang. *Dynamical Theory of Crystal Lattices*. Oxford University Press, Oxford, 1954.
- [79] Félix Mouhat and François-Xavier Coudert. Necessary and sufficient elastic stability conditions in various crystal systems. *Physical Review B*, 90:224104, 2014.
- [80] Atsushi Togo, Laurent Chaput, Isao Tanaka, and Gilles Hug. First-principles phonon calculations of thermal expansion in  $\text{ti}_3\text{sic}_2$ ,  $\text{ti}_3\text{alc}_2$ , and  $\text{ti}_3\text{gec}_2$ . *Physical Review B*, 81:174301, 2010. QHA methodology for thermal expansion.
- [81] Atsushi Togo and Isao Tanaka. First principles phonon calculations in materials science. *Scripta Materialia*, 108:1–5, 2015. Phonopy software for phonon calculations.
- [82] Pascal Vinet, John Ferrante, James R. Smith, and James H. Rose. A universal equation of state for solids. *Journal of Physics C: Solid State Physics*, 19(20):L467–L473, 1986. Vinet equation of state.